Title
Effect of polymer conjugation and nanotopography on implant compatibility and wound healing

Permalink
https://escholarship.org/uc/item/7g6957fj

Author
Muthusubramaniam, Lalitha

Publication Date
2013

Peer reviewed|Thesis/dissertation

Effect of polymer conjugation and nanotopography on implant compatibility and

wound healing

by

Lalitha Muthusubramaniam

DISSERTATION

Submitted in partial satisfaction of the requirements for the degree of

DOCTOR OF PHILOSOPHY

in

Bioengineering

in the

GRADUATE DIVISION

of the

UNIVERSITY OF CALIFORNIA, SAN FRANCISCO

AND

UNIVERSITY OF CALIFORNIA. BERKELEY

ACKNOWLEDGEMENTS

To my advisor, Tejal Desai, my sincere thanks for being so supportive of my interests in research and in life. Joining this lab was one of the best decisions I made in graduate school, and a big reason for this was your constant support over the last few years.

To my lab mates who were the other big reason for why this lab was an awesome place to work in. There are far too many to name, but they are all people who filled my time here with great memories. I also value the friendships formed with folks outside the lab – students from my cohort, from the Graduate Students Association and collaborators in various groups both within and outside UCSF.

To my qualification and dissertation committee members, thank you for suggestions and help with my dissertation.

To my family who mean everything to me - my mother, who always encouraged me to pursue my interests; my father, for his words of advice; my wonderful son Keshav, who makes me learn something new about life everyday; my sister and my close friends - a simple thank you for all the times you listened to me and encouraged me.

And last but anything but least, to my husband Vasanth, who not only encouraged me to pursue my PhD, but constantly stood by my side and made it easier to keep going when the times were tough. Thank you for the numerous sacrifices you made during this time so that I could achieve my goal.

The text of this dissertation is a reprint of the material as it appears in the following papers:

Muthusubramaniam L, Lowe R, Fissell WH, Li L, Marchant RE, Desai TA, Roy S. Hemocompatibility of silicon-based substrates for biomedical implant applications. Ann Biomed Eng. 2011 39(4):1296-305.

Muthusubramaniam L, Peng L, Zaitseva T, Paukshto M, Martin GR, Desai TA. Collagen fibril diameter and alignment promote the quiescent keratocyte phenotype. J Biomed Mater Res A. 2012 100(3):613-21.

Muthusubramaniam L, Zaitseva T, Paukshto M, Martin GR, Desai TA. Effect of collagen nanotopography on keloid proliferation and matrix synthesis: Implications for dermal wound healing. *Manuscript under submission.*

ABSTRACT

This dissertation focuses on two aspects that present challenges for a broad range of implantable devices and transplants – blood compatibility and wound healing properties of biomaterials. In the first chapter, we examined the hemocompatibility of surface modified silicon substrates used in renal replacement devices. Our reports showed that the polymer conjugated silicon samples reduced platelet attachment and activation to levels comparable to that on Teflon, a material commonly used in medical implant devices. Our findings suggest that surface modified silicon substrates could be used to develop miniaturized implants for renal replacement therapies.

In the second chapter, we investigated how collagen nanotopography affects wound healing in the cornea. The presence of nanopatterned collagen fibrils was shown to promote the appearance of the healthy keratocyte phenotype and attenuate the fibrotic myofibroblast phenotype. In addition, collagen nanotopography also had an effect on matrix synthesis. These results have significant implications for the design of tissue engineered corneal substitutes and for promoting regenerative wound healing in the cornea.

In the third chapter, we focused on wound healing in the skin, particularly in the case of keloid scars. Keloids are locally aggressive dermal scars formed as a result of abnormal wound healing. They are characterized by excessive fibroblast proliferation and matrix production. An effective treatment for keloids is yet to be established due to a high rate of recurrence. Our results showed that collagen fibril alignment reduced cell proliferation and matrix synthesis in fibroblasts derived from keloid, scar and healthy

dermal tissue. This data suggests that aligned collagen fibrils could be used to develop dermal patches that reduce the recurrence of keloids and aid in the design of an effective therapy for keloid management. The recurring theme in both the cornea and keloid studies is that matrix architecture could be used to effectively manipulate cell response to direct regenerative wound healing. Collectively our findings show that physical cues such as matrix topography could be used to improve the anti-fibrotic properties of biomaterials and aid in the design of tissue engineered implants for various clinical applications.

TABLE OF CONTENTS

LIST OF TABLES

LIST OF FIGURES

CHAPTER 1: Introduction

Implant biocompatibility and wound healing are two major challenges in the field of biomaterials research. Currently used biomaterials often cause blood coagulation and/or fibrosis, resulting in poor hemocompatibility and scarring. This dissertation attempts to address these challenges using two different approaches: (1) Surface modification of a synthetic material such as silicon using polymer conjugation to improve blood compatibility and (2) Fabricating a nanopatterned scaffold using a biological material such as collagen to reduce fibrotic response. In Chapter 2, the first approach is described wherein we examine the blood compatibility of a synthetic material such as silicon for use in renal implantable devices. When foreign surfaces come in contact with blood, there are a variety of adverse reactions that can occur such as platelet and protein adhesion, which lead to surface clotting and loss of implant function. To counter this, we modified the implant surface with biocompatible polymer coatings and examined the effect of these modifications on the hemocompatibility of the substrates. Our tests revealed that surface-modified silicon substrates showed low levels of platelet attachment and activation, in addition to showing reduced coagulation and complement activation. This suggests that these substrates could be used for the development of membranes for use in implantable renal devices.

In Chapters 3 and 4, the second approach is described wherein we manipulate the nanotopography of a biopolymer such as collagen, to modulate cell response and promote wound healing. In Chapter 3, we examined the properties of a biomimetic substrate composed of collagen nanofibrils with respect to corneal wound healing. For this study, we used three collagen nanopatterned substrates – the first made of 30 nm aligned fibrils,

which mimic the collagen arrangement seen in the cornea. The second and third substrates were composed of 300 nm aligned fibrils, and 30 nm non-aligned fibrils, and were selected to investigate the effect of fibril diameter and alignment on corneal fibroblast phenotype and matrix synthesis, both of which are linked to corneal wound healing. Our studies showed that collagen nanotopography promoted the quiescent corneal fibroblast phenotype, downregulated the fibrotic phenotype and had an effect on matrix production. These results have significant implications for the fabrication of a tissue-engineered implant that could promote regenerative healing of the cornea.

In Chapter 4, we decided to extend the corneal studies to examine wound healing in other types of tissue such as skin. To this end, we examined the anti-fibrotic properties of the nanopatterned collagen substrates for dermal wound healing, specifically in the case of keloid scars. Keloids are benign dermal tumors defined by excessive fibroblast proliferation and matrix synthesis. The inner and outer regions of a keloid display a difference in collagen architecture and also differ in the rate of cell proliferation, indicating the importance of collagen topography in keloid scar growth and maturation. Our experiments showed that the presence of aligned collagen fibrils reduced fibroblast proliferation and matrix production, and also reduced the appearance of the fibrotic myofibroblast phenotype. Thus collagen nanotopography could be used for the development of a dermal patch that would limit scar growth and prevent keloid recurrence. A collagen patch would be fully biocompatible and non-invasive and thus aid in the design of a safe and effective therapy for keloid management.

CHAPTER 2. Hemocompatibility of Silicon-based Implant Materials

2.1 Background

Silicon based materials are being used in the fabrication of a wide range of biomedical devices for diagnostic and therapeutic applications. These include devices for drug delivery[1], neural electrodes[2] and implantable sensors[3], many of which are being considered for use within the body. One such promising technology is the development of miniaturized renal replacement devices using silicon nanoporous membranes.[4] Such devices allow for extended dialysis each day leading to better outcomes and improved quality of life for patients with kidney failure. Current technologies make use of polydisperse polymer membranes which are limited by the need for high driving pressures for circulation and clearance. In contrast, silicon membranes with highly uniform pore sizes fabricated using MEMS (microelectromechanical systems) technology offer a promising approach for the production of miniaturized, high-performance renal replacement systems.[5] Moreover, these membranes have been shown to support the growth and function of human renal proximal tubule cells indicating that they do not exhibit cytotoxicity.[4]

However, it is important that the single crystal silicon substrates display minimal adverse reactions in terms of blood compatibility (low surface coagulation, complement and/or platelet activation and thrombosis adhesion) for effective use as the membrane material. Blood material interactions are especially important for hemodialysis due to the chronic exposure of blood to the membrane surface during treatment.[6] Here we evaluate the blood compatibility of solid silicon substrates with and without surface modification

by polymer conjugation. We have examined 4 types of surface modification in this study, all of which have been shown to improve biocompatibility by preventing protein and/or platelet adhesion on the underlying surface. The first 2 are polyethylene glycol (PEG) conjugated to the surface using liquid[7] and vapor based deposition techniques, respectively. PEG has been shown to reduce non-specific protein adsorption and fouling on silicon surfaces.[8] Solvent-free vapor deposition of PEG has been demonstrated to reduce protein adsorption by up to 80% on silicon-based surfaces.[9] Furthermore, PEG films have shown long-term resistance to biofouling by reducing protein adsorption on silicon surfaces for up to 4 weeks under aqueous *in vivo* like conditions.[10]

The third polymer is a glycolayx-mimetic dextran-modified polyvinylamine (PVAm) surfactant which has been shown to reduce platelet adhesion.[11] A zwitterionic polymer, polysulfobetaine methacrylate (pSBMA), shown to have good antifouling properties, was the fourth surface modification tested in the study.[12] Additionally, polysilicon substrates used in MEMS fabrication to create uniformly porous membranes[8] were also included in this study.

Previous studies that have examined blood compatibility of silicon primarily focused on platelet adhesion tests of silicon-based substrates under static conditions[13,14]. Here we extend these studies to investigate various aspects of hemocompatibility such as coagulation and complement activation, in addition to platelet activation. Accordingly, the surfaces were incubated with freshly drawn anticoagulated human whole blood or platelet-rich plasma (PRP) and tested for 4 different markers reflecting the following test categories – coagulation (thrombin-antithrombin complex, TAT generation), complement

activation (formation of activated complement protein C3a), platelet activation (expression of P-selectin, CD62P), and platelet adhesion.

Hemocompatibility of the silicon based substrates was compared to Teflon (polytetrafluroethylene, PTFE) and medical grade stainless steel, 2 substrates that are routinely used in various medical implants.[15,16] Both these surfaces display excellent blood compatibility[17,18] and serve as negative controls in this study. Diethylaminoethyl (DEAE) cellulose, a polymer used in commercially available dialysis membranes[6] was also tested to compare the performance of the silicon-based substrates with a conventional dialyzer material. Previously it has been shown that DEAE cellulose has advantages in terms of low platelet and complement activation, but exhibits high levels of TAT generation.[6,19] Thus, it is not the ideal choice of dialyzer material with respect to surface coagulation. Other polymer membranes such as polysulfone have more favorable coagulation properties in comparison to DEAE cellulose.[6] However, this material was selected as the reference substrate because it could also serve as a positive control in our experiments. Adenosine diphosphate (ADP) is a known agonist of platelet activation.[20] Upon activation, ADP is released from the dense granules of platelets, and aids in platelet aggregation and further activation. Hence, ADP was used as a positive control for platelet activation studies.

2.2. Materials and Methods

Materials

All chemicals were purchased from Sigma Aldrich (St. Louis, MO, USA) unless specified. Poly(*N*-vinyl dextran aldonamide-co-*N*-vinyl hexanoamide) (PVAm-Dex/Hex) was purchased from Greatbatch, Inc. (Clarence, NY, USA) and 2-bromo-2-methyl-*N*-3-[(trimethoxysilyl)propyl]-propanamide (BrTMOS) was synthesized according to literature.[21] Virgin, prime-grade, single side polished, 500 μm thick, <100>-oriented, n-type, silicon wafers were used in the study. Deposition of polysilicon was performed at Cleveland Clinic. DEAE cellulose (Whatman, Piscataway, NJ, USA), Teflon (Scientific Commodities, Lake Havasu City, Arizona, USA) and stainless steel (Feather Safety Razor, Medical Division, Kita-ku, Osaka, Japan) were used as reference materials.

Substrate preparation

Liquid-based deposition of polyethylene glycol (PEG) on silicon was performed as described in previously published reports.[7] Briefly, the single crystal silicon substrates were first sonicated in 70% ethanol for 10 min and then dried with nitrogen. Substrates were then oxidized in a 20:80 hydrogen peroxide (30%) and sulfuric acid (96%) mixture for 10 min at 120 °C. Substrates were then washed and sonicated for 10 min in deionized water and dried with nitrogen. Immediately, silicon substrates were immersed in a solution of 3 mM 2-[methoxy(polyethyleneoxy)propyl]trimethoxysilane in toluene for 18 hr at room temperature. Finally, the substrates were extensively washed with toluene, ethanol and deionized water, before being dried with nitrogen to prepare the PEG conjugated substrates.

Vapor-based deposition of PEG on silicon was performed at UCSF according to protocols developed in our laboratory. Single crystal silicon substrates were cleaned with a 3:1 sulfuric acid:hydrogen peroxide solution, rinsed in deionized water, and dried with nitrogen. Silicon pieces were then treated with oxygen plasma (200W, 0.5 mTorr) for 5 minutes prior to being placed in the Teflon deposition chamber. The deposition chamber was purged with nitrogen, and a hot plate was used to maintain silicon surface temperature of 120°C. [2-methoxy(polyethyleneoxy)propyl]trimethoxysilane (PEG-silane) was vaporized at 250°C in a closed stainless steel loop and subsequently released into the deposition chamber. 4 vapor exposures for 30 min each were performed before silicon samples were removed for use.

PVAm modified silicon substrates were prepared at Cleveland Clinic according to protocols published in our laboratory.[22] Briefly, single crystal silicon wafers were plasma cleaned and placed in a solution of octadecyltrichlorosilane for 30 min. The wafers were then washed twice with dried chloroform before immersion into an aqueous solution of PVAm-Dex/Hex for 24 h. The substrates were finally rinsed with deionized water and air dried to prepare the PVAm modified silicon substrates.

The pSBMA modified substrates were also fabricated at Cleveland Clinic using protocols published by our laboratory.[21] Cleaned wafers of single crystal silicon were placed in an anhydrous bicyclohexyl solution of BrTMOS for 2 h, rinsed, air dried and then placed in a flask under nitrogen. Polymerization was carried out using a solution of [2-(methacryloyloxy)ethyl]dimethyl-(3-sulfopropyl)ammonium hydroxide monomer (SBMA) and 2,2'-bipyridyl (BPY) dissolved in a degassed solution of methanol and deionized water, to which copper(II) bromide and copper(I) bromide had been added. The

substrates were then rinsed with and stored in deionized water overnight and then air dried for use in the study.

The surface of a silicon wafer oxidizes to form silicon dioxide when exposed to air. Our unmodified silicon surfaces are hence Si/SiO_2 surfaces. The unmodified silicon substrates were cleaned with piranha (3:1 H_2SO_4/H_2O_2 mixture) and dried with nitrogen before use. All substrates (except DEAE cellulose) were rinsed with 70% ethanol and dried before use. The substrates were all sterilized using UV radiation for 5 minutes prior to blood or plasma incubation.

Blood collection

Blood was drawn at the UCSF Blood Center from healthy human donors using 3.8% citrate (Fisher Scientific, Pittsburgh, PA, USA) or 17 IU/ml heparin (Fisher Scientific, Pittsburgh, PA, USA) as anticoagulant. Informed consent was obtained from donors prior to blood donation. Heparin is a commonly used anticoagulant in blood compatibility testing of biomaterials *in vitro*[23,24] and was selected as the anticoagulant for TAT generation studies. Unfractionated heparin (UFH) binds antithrombin and converts it into a more efficient inhibitor of thrombin and other coagulation factors such as factor Xa, factor IXa and factor XIIa.[25] At high concentrations, heparin binds heparin cofactor II to inhibit thrombin independent of antithrombin; however, it also binds to platelets and induces their aggregation. Heparin also binds anaphylotoxins such as the complement protein C3a.[26] Sodium citrate neutralizes coagulation factor activation. Since citrate is a calcium chelator, it reduces the ionized calcium concentration in plasma leading to enhanced GPIIb/IIIa binding and inhibition of platelet aggregation.[27] Thus citrate does

not cause spontaneous platelet activation *in vitro* and any activation that is seen is due to the surface of the biomaterial itself. For these reasons, citrate was selected for the platelet and complement activation studies.

Blood samples were stored on ice until the start of experiments based on previously published reports in literature,[28,29] and in accordance with the guidelines of the International Standard ISO 10993 Part 4 – Selection of tests for interactions with blood.[30] All blood samples were handled in a similar manner and stored on ice for an equivalent amount of time (60 ± 5 min). Whole blood was centrifuged at 1000 rpm for 10 min at room temperature to obtain PRP for platelet adhesion studies. Platelet counts were obtained using a Hemavet950 (Drew Scientific, Oxford, CT, USA).

Blood incubation and analysis

Flow is the natural state of blood and flow studies are the ideal representation of conditions *vivo*. Our experiments conducted under non-perfusion conditions are preliminary studies indicative of data obtained with flow-based studies. In flow based systems, blood is exposed to additional foreign material such as tubing and shear stress due to pumping, all of which have been shown to increase the activation of blood components.[17] Streller et al. have shown that data obtained under non-flow conditions are representative of flow-based studies using control substrates such as Teflon, glass and polyethersulfone. Considering these aspects, we decided to conduct preliminary studies under static conditions to examine the relative difference in activation levels between bare silicon and surface modified silicon substrates. The substrates were however incubated on a gentle shaker (50 shakes per min) to avoid sedimentation of platelets.[23,24]

400 µl of whole blood from 3 donors was dispensed onto the substrates (10 mm X 10 mm) placed in 24-well tissue culture polystyrene (TCPS) microplates. 4 replicates were used for each donor for all substrates except polysilicon, where only 3 replicates were available for one of the donors due to inadvertent error in sample handling. For the C3a studies, substrates were mounted on Teflon spacers placed on tissue culture dishes to minimize possible activation from TCPS (Supplementary Figure S2.1). The substrates were incubated for 2 h at 37 °C on a gentle shaker. Commercial ELISAs were used to characterize TAT generation (Enzygnost TAT micro, Siemens Healthcare Diagnostics, Deerfield, IL, USA) and C3a formation (Human C3a ELISA Kit, BD Biosciences, San Jose, CA, USA). Blood samples were mixed with specific inhibitors and centrifuged to collect plasma according to the manufacturer's protocols. Plasma samples were frozen at -70 ºC until further analysis.

Surface analysis after incubation

Platelet adhesion and activation was visualized using immunofluorescence staining for the platelet marker, CD41 (Abcam) and activated platelet marker, CD62P (Abcam). 200 µl of PRP (3.3 X 10^5 platelets/ µL) from 1 donor was dispensed onto the substrates (10 mm X 10 mm) mounted on Teflon spacers and incubated for 2 h at 37 °C on a gentle shaker. 3 replicates were used for all substrates except polysilicon, where only 2 replicates were available due to inadvertent error in sample handling. The platelets were treated with ADP in solution. ADP (40 µM final concentration in PRP) was added to the platelet-rich plasma and dispensed on single crystal silicon (10 mm X 10 mm) in triplicate for use as the positive control. After 2 h, PRP was removed and the substrates were transferred to a 24-well plate and washed with phosphate-buffered saline (PBS).

The platelets were fixed in 4% paraformaldehyde (Fisher Scientific) for 15 min, and blocked in 1% bovine serum albumin for 30 min. Platelets were double labeled as follows: substrates were first incubated with antihuman CD62P mouse monoclonal antibody, diluted 1:50 in PBS for 60 min followed by Alexa Fluor 546 donkey anti-mouse antibody (Invitrogen) diluted 1:100 in PBS for 60 min. Finally the samples were incubated with antihuman CD41 FITC labeled mouse monoclonal antibody diluted 1:300 in PBS for 60 min. Four images were acquired per replicate using a NikonEclipse Ti-E motorized inverted microscope to obtain a total of 12 images per substrate. Data analysis was performed using Fiji, an Open Source image analysis package based on ImageJ (http://pacific.mpi-cbg.de/).

Statistical analysis

Statistically significant differences were estimated using analysis of variance (ANOVA) tests. For group differences shown to be significant by ANOVA, sequential Holm t-tests were performed to detect differences between specific pairs of substrates.

2.3 Results and Discussion

Surface Coagulation

Activated thrombin is inhibited by antithrombin-III to form a proteinase/inhibitor complex (TAT), the concentration of which is used as a measure of thrombin activation and coagulation.[17] Generation of TAT complex after whole blood incubation with the substrates was therefore determined to evaluate surface coagulation. As seen from Figure 2.1, the most striking difference is that TAT generation is drastically reduced (~25 to 50

fold, p<0.001) on the silicon-based substrates when compared to DEAE cellulose. This indicates that the silicon based substrates display superior anticoagulation properties when compared to the highly thrombogenic DEAE cellulose surface. Previously it has been shown that DEAE cellulose exhibits high levels of TAT generation.[6,19] This is in good agreement with our data where DEAE cellulose acts as a positive control exhibiting high levels of TAT formation.

Most importantly, there is no significant difference in TAT generation with the single crystal silicon, modified silicon and polysilicon substrates when compared to Teflon and stainless steel. Thus, the silicon based substrates display excellent anticoagulation, comparable to the negative control substrates.
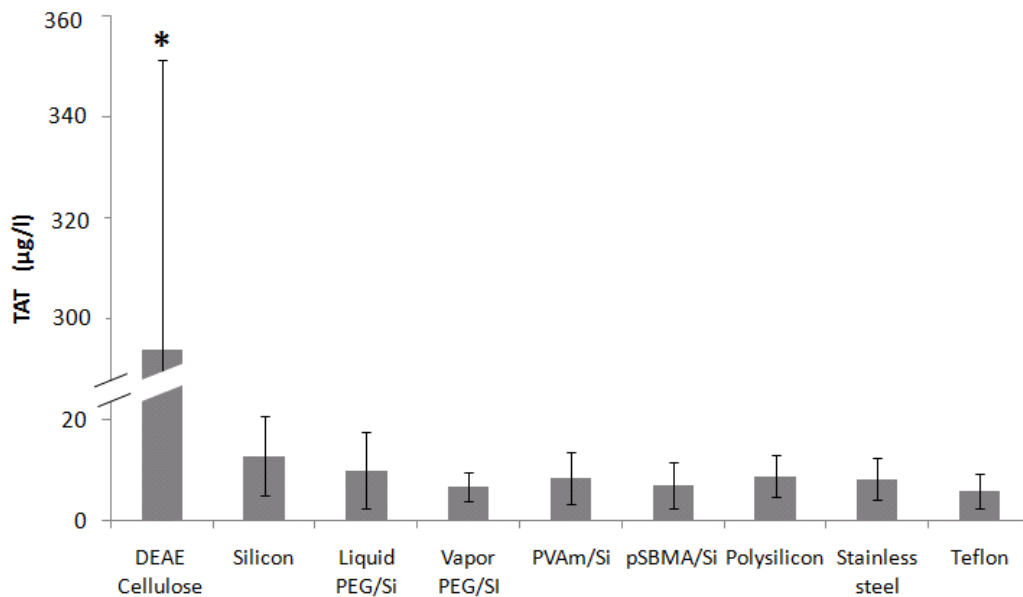
Figure 2.1: Surface coagulation presented as a measure of TAT generation after whole blood incubation with the substrates. Data is presented as average ± standard deviation. *p <0.001 vs. Teflon.

Complement Activation

C3a anaphylatoxin is produced upon activation of the classical or alternate complement pathways. The amount of C3a formed after whole blood incubation with the substrates is therefore used as a measure of complement activation.[31] As seen from Figure 2.2, C3a formation on the silicon-based substrates is substantially reduced (~3 to 4 fold, $p<0.001$) in comparison to DEAE cellulose. Previous studies have shown that modification of cellulose by the incorporation of DEAE groups offers certain advantages such as reduced complement activation.[6,19] However, the silicon substrates exhibit even lower levels of C3a formation, indicating that they compare even more favorably than DEAE cellulose in terms of complement activation.
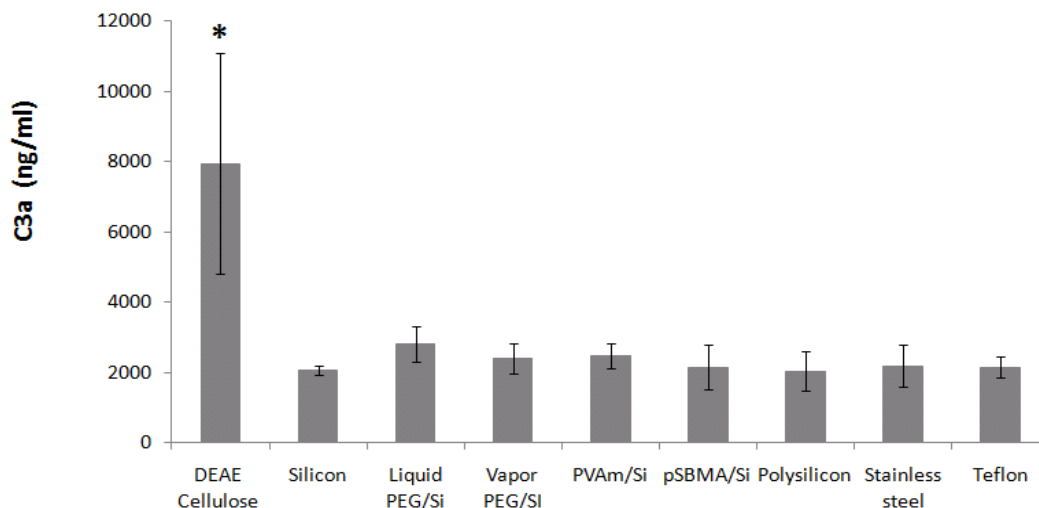
Figure 2.2: Complement activation presented as amount of C3a formed after whole blood incubation with the substrates. Data is presented as average ± standard deviation. *$p<0.001$ vs. Teflon.

More importantly, there is no significant difference in C3a formation between the single crystal silicon, polysilicon and modified silicon substrates with respect to Teflon and stainless steel indicating that these substrates do not exhibit significant complement activation.

13

Platelet Adhesion and Activation

CD41 is an integrin heterodimer consisting of a heavy chain (GPIIb alpha) and a light chain (GPIIb beta) that is expressed on the surface of platelets. The alpha IIb chain forms a platelet glycoprotein complex with another molecule, CD61 and thus aids in platelet adhesion and aggregation. The CD62P antigen is a member of the selectin family of cellular adhesion molecules located in the storage granules of platelets. Upon activation, CD62P is released and stably expressed on the surface of activated platelets. Thus CD41 and CD62P can be used as markers for platelet adhesion and activation, respectively.[32] The fibrous texture of DEAE cellulose made it difficult to visualize platelet staining on this surface. Hence ADP, a known platelet activator, was used as the positive control for this study. Previous studies have established Teflon as a material that displays minimal platelet activation and thrombosis.[17] Hence Teflon was selected as the as the negative control for further studies with platelet activation.

In this work, blood samples were stored on ice based on protocols from previously published reports in literature.[28,29] Blood storage on ice is also in accordance with the guidelines of the International Standard ISO 10993 Part 4 – Selection of tests for interactions with blood.[30] Bergseth et al., report that the ideal conditions for storing blood samples collected for platelet activation studies is to place them on ice for 30 min.[28] Another study that specifically looked at optimizing blood storage conditions reported that the percentage of CD62P positive platelets does not change in anticoagulated blood samples stored at 4 ºC over a period of 180 min,[29] indicating that chilling does not change P-selectin levels at least over the time period relevant to our studies. In contrast, room temperature storage leads to the secretion of metabolic products such as lactate resulting

in low pH and decreased platelet viability[33,34]. At room temperature, platelets get activated as indicated by the secretion of beta-thromboglobulin, platelet factor-4 and P-selectin, all of which are known markers for platelet activation. For these aforementioned reasons, the choice was made to store the blood samples on ice until the start of experiments. Additionally, we observed minimal to no platelet activation on the surface modified silicon substrates and Teflon control (Figure 2.4, d - g). Thus, it is unlikely that platelet activation is caused by storage of blood samples on ice.

As seen in Figure 2.3, single crystal silicon and polysilicon display extensive platelet adhesion and activation as shown by labeling for CD41 (green), CD62P (red) and colocalization (Figure 2.4 a, b). However, platelet spreading on these 2 substrates is still considerably lesser compared to the ADP/ silicon substrate (Figure 2.4c). Also, the ratio of activated platelets on ADP/ silicon (0.92) is higher than that on either bare silicon (0.8) or polysilicon (0.5), respectively (Figure 2.5). Increase in platelet spreading has been correlated with higher levels of platelet activation.[14] Thus the dramatic increase in platelet size (~10 fold as seen in Figure 2.5, $p < 0.001$) on ADP/ silicon compared to bare silicon or polysilicon establishes ADP as a good positive control for this study. Platelet spreading on the ADP/ silicon surface also contributes to the lower platelet count per unit area as seen in Figure 2.5.
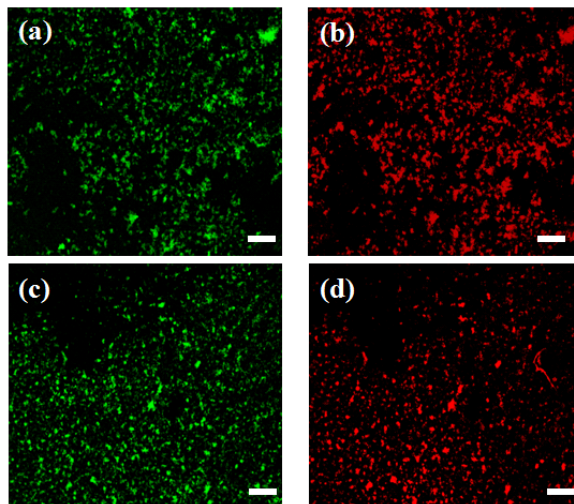
Figure 2.3: Representative images showing platelet adhesion and activation after incubation with PRP as visualized by immunofluorescence staining for CD41 (in green, platelet marker) and CD62P (in red, activated platelet marker). (a) Bare silicon substrate showing the FITC-labeled CD41 channel alone, (b) bare silicon substrate showing the Alexa 547-labeled CD62P channel alone,(c) and (d) are corresponding images in bare polysilicon substrate. Scale bars represent 10 μm.

Notably, the polymer conjugated silicon substrates show minimal to no platelet coverage compared to the unmodified single crystal silicon substrate (Figure 2.4, d - g). Platelet counts (both activated and non-activated) are also significantly lower on these surfaces compared to unmodified silicon as seen in Figure 2.5 ($p<0.001$). This indicates that surface modification significantly reduces platelet adhesion and activation on the silicon surface. Of the 4 types of modifications that were tested, pSBMA alone shows slightly higher levels of platelet adhesion and activation as seen from the platelet counts and the mean platelet size in Figure 2.5. However, platelet counts on the pSBMA substrate are still 8-fold lower compared to that of unmodified silicon substrate.
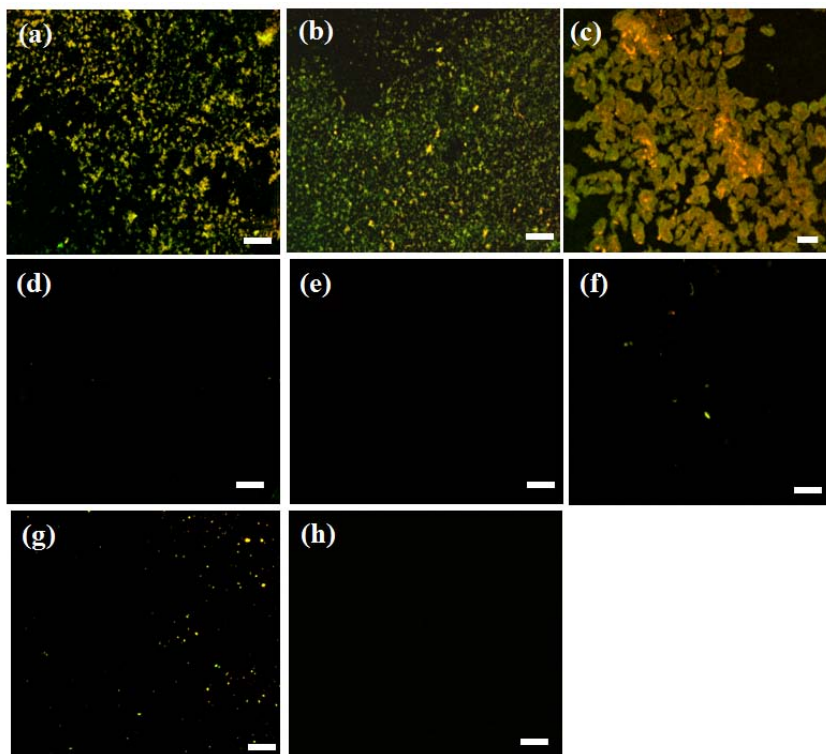
Figure 2.4: Superimposed images of the FITC-labeled CD41 (green) and Alexa 547-labeled CD62P (red) show colocalization of platelet adhesion and activation as seen in yellow: (a) Bare silicon, (b) bare polysilicon, (c) ADP/silicon, (d) liquid PEG/silicon, (e) vapor PEG/silicon, (f) PVAm/silicon, (g) pSBMA/silicon, and (h) Teflon. Scale bars represent 10 μm.

Previously it has been shown that PEG modification significantly reduces protein adsorption and thrombosis on silicon-based substrates.[8,9] Moreover, PEG films have been shown to retain their ability to reduce protein fouling for up to 4 weeks under aqueous *in vivo* like conditions.[10] Platelet adhesion on PVAm coated polycarbonate disks has been shown to be ~90% less than that of uncoated disks.[11] pSBMA grafted surfaces have also been shown to reduce platelet adhesion and activation.[12] These results are in good agreement with our data indicating that surface modification can be used to significantly improve the hemocompatibility of silicon for implant devices. Of considerable interest is

the fact that platelet adhesion and activation levels on the modified silicon substrates (with the exception of pSBMA) are not significantly different from that of Teflon (Figure 2.4h). This result is encouraging as it indicates that surface modification reduces platelet activation on silicon to levels comparable to that of Teflon, a material that is extensively used in medical implant devices.
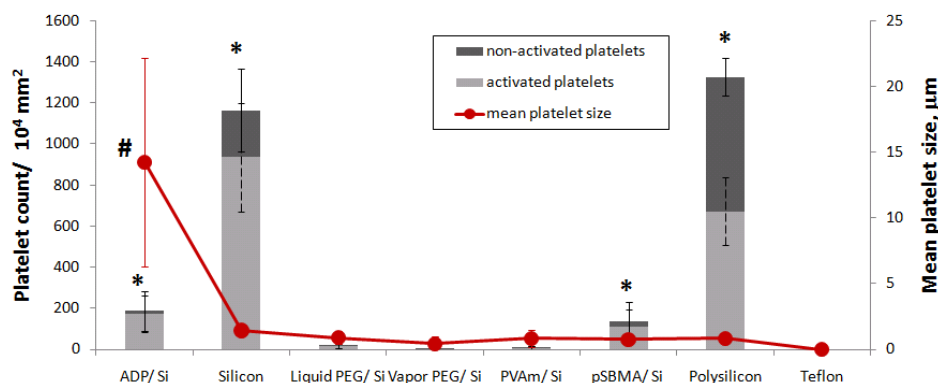
Figure 2.5: Platelet adhesion and activation after incubation of substrates with PRP: The vertical axis on the left represents the number of activated and non-activated platelets attached to the substrate as visualized by immunofluorescence staining for CD41(platelet marker) and CD62P (activated platelet marker). Data is presented as average ± standard deviation of 12 images. *p <0.001 vs. corresponding platelet counts in vapor PEG/silicon. The vertical axis on the right represents mean platelet size. Data is presented as average ± 95% confidence interval of 12 images. #p <0.001 vs. corresponding size in vapor PEG/silicon. Teflon could not be used as reference because platelet count on Teflon was zero.

Pilot studies conducted in rats using silicon implants with and without PEG conjugation have shown that PEG conjugated silicon implants showed no thrombus formation compared to bare silicon implants which had significant adherent thrombi.[35] This data is in excellent agreement with our studies showing that surface modification using polymers such as PEG significantly reduces platelet adhesion and activation on silicon. While these results are very encouraging, these preliminary studies need to be

extended to examine long-term blood compatibility of silicon membranes under flow-based conditions that are relevant to the end application of dialysis. Future work should also focus on investigating different markers of hemocompatibility *in vivo* to evaluate the feasibility of silicon membranes for use in implantable renal replacement systems.

Conclusion

Any device that is brought into contact with blood causes adverse reactions thus compromising the hemocompatibility of the device. Such reactions are particularly challenging in the case of hemodialyzers which come into chronic contact with blood. It is therefore very important to evaluate the blood compatibility of silicon surfaces before they can be used in the development of implantable renal replacement units. Our studies show that unmodified single crystal silicon and polysilicon substrates display low levels of coagulation and complement activation, comparable to that of Teflon and stainless steel – 2 materials extensively used in implant applications. Both these surfaces also perform considerably better in these aspects when compared to DEAE cellulose, a commercially available material used in dialysis membranes. The unmodified silicon substrates however display significantly higher levels of platelet activation compared to Teflon, although these values are still substantially lower than that with ADP (~10-fold), a known agonist of platelet activation.

Of considerable interest is the fact that silicon substrates modified with PEG and PVAm polymers showed excellent performance comparable to Teflon in all 4 aspects of hemocompatibility - surface coagulation, complement and platelet activation and

adhesion, respectively. Thus surface modification improves the blood compatibility of silicon to levels comparable to medical grade implant materials such as Teflon. All the surface modifications that were tested (PEG, PVAm and pSBMA) were also far superior to DEAE cellulose in terms of coagulation and complement activation. This is encouraging as it suggests that surface modified silicon substrates have the potential to perform significantly better than some of the currently available materials used in dialyzers. Collectively, our results demonstrate that the surface modified silicon substrates may be used in the development of membranes for implantable biomedical devices.

CHAPTER 3. Effect of collagen nanotopography on corneal wound healing

3.1 Background

Corneal disease is a major cause of blindness affecting more than 10 million people worldwide.[36] Corneal transplants are currently the only available treatment to restore vision, with approximately 40,000 transplants being performed in the Unites States each year.[37] Shortcomings of the procedure include immune rejections, infections and donor shortages. This has motivated several attempts to develop tissue engineered corneal replacements.[38,39,40] The cornea has three main layers – the epithelium, endothelium and stroma.[36] The stroma contains quiescent cells called keratocytes that reside within uniformly aligned collagen fibrils, 30 – 35 nm in diameter (Figure S3.1). Uniformity of fibril diameter and alignment are thought to be instrumental in maintaining transparency of the cornea. The fibrils are further arranged in alternating arrays called lamellae (1 – 2 μm in thickness) which are stacked orthogonally leading to a lattice like arrangement which provides mechanical strength to the cornea. The difficulty in recreating the organized nanoscale architecture of the stroma has been one of the primary impediments to the successful production of a tissue engineered corneal replacement.

When the cornea sustains injury such as an abrasion which disrupts the extracellular matrix (ECM), the quiescent corneal keratocytes adjacent to the wound undergo apoptosis.[41] Keratocytes adjacent to the apoptotic region transform into repair cells including activated fibroblasts and myofibroblasts, the latter of which are characterized by the expression of α–smooth muscle actin (SMA). These cells invade the wound region and attempt to repair the injury site by secreting matrix proteins such as

collagen 1 (COL1), collagen 3 (COL3), fibronectin (FN) and biglycan. However, the matrix proteins that are secreted form a disorganized matrix of irregular scar tissue with decreased transparency. This decrease in transparency is exacerbated by the loss of corneal crystallins, such as transketolase (TKT). Corneal crystallins are responsible for index-matching the cell body of the keratocyte with the stroma and improving light transmission through the cells.[42] Quiescent cells express corneal crystallins which improve the transparency of the cornea, while activated cells such as myofibroblasts have reduced expression of crystallin proteins. Interestingly, in the case of corneal burns or freeze injuries where the ECM is left intact, quiescent corneal keratocytes proliferate and repopulate the wound without phenotype switching and without scar formation.[43] Thus the integrity of the matrix and the nanoscale arrangement of the collagen fibrils seem to be important for regenerative healing of the cornea after injury.

Previous studies have shown that corneal fibroblasts align and migrate differentially on substrates with different topographical features.[44,45] Phu *et al.* have shown that corneal fibroblasts cultured on aligned collagen fibers down-regulate SMA compared to cells grown on unaligned fibers or tissue culture polystyrene (TCPS).[37] However, the effect of fibril diameter or alignment on the expression of corneal crystallins and matrix proteins has not been investigated thus far. The objective of this study was to evaluate how the topography of collagen fibrils that keratocytes encounter *in vivo* affects cell phenotype, matrix synthesis, and potentially corneal wound healing after injury. We examined the individual contribution of two properties of the collagen fibrils - namely, fibril diameter and alignment, and their effect on cell phenotype and matrix production. To this end, three types of nanofiber scaffolds with collagen fibrils of varying

topography - 30 nm aligned fibrils (30A), 300 nm or larger, aligned fibrils (300A), and 30 nm nonaligned fibrils (30NA), were assembled on glass substrates using a nanoweaving technology developed by Fibralign Corporation. The 30A substrates were selected as a representative arrangement of collagen fibrils *in vivo*. The 300A substrates were chosen to study the effect of fibril diameter, while the 30NA substrates were selected to investigate the effect of fibril alignment on cell response, respectively. Flat glass substrates coated with bovine collagen, type I (FC) were used as controls that present no predetermined topography to the cells. Bovine corneal fibroblasts were cultured on three nanofiber scaffolds (30A, 300A and 30NA) and the flat collagen coated controls. Cell morphology of the corneal fibroblasts was visualized by staining for f-actin and the nucleus using spectral confocal microscopy. Gene expression levels of six proteins – TKT, SMA, collagens 1 and 3, fibronectin, and biglycan were measured to evaluate the effect of nanotopography on matrix synthesis and cell phenotype.

3.2. Materials and Methods

Corneal fibroblast isolation and cell culture

Bovine corneal fibroblast isolation was performed based on a previously published protocol.[46] Corneal buttons were isolated from bovine eyes (Manna Foods, Oakland, CA, USA) by making incisions around the corneal while excluding the scleral and limbal regions. The posterior surface of the buttons was scraped to remove endothelial cells. Buttons were then immersed in a Dispase I solution at 100 mg/ml (Roche, Indianapolis, IN, USA) for four hours and epithelial cells were removed using repeated scalpel strokes while the buttons were still immersed in the Dispase solution.

After rinsing with phosphate buffered saline (PBS), the corneal buttons were cut in half and placed on a fibronectin coated plate. Fibronectin was obtained from Athena Environmental Sciences (Baltimore, MD, USA) and plates were coated according to the manufacturer's instructions. The corneal buttons were then covered with corneal fibroblast complete media (DMEM + 10% fetal bovine serum, FBS +1% Penicillin-Streptomycin solution + 100 mg/L sodium pyruvate), where FBS is an activator of the corneal fibroblast phenotype.[47] The corneas were then incubated at 37 °C and 5% CO_2 until the plates were 85% confluent. Then, the corneal fibroblasts were harvested using trypsin (2.5g/L in 2.5 mM EDTA) and resuspended in complete media. Corneal fibroblasts were cultured in fibronectin coated tissue culture flasks in complete media that was changed three times a week. Cells were split approximately once or twice a week and cultured in a humidified 95% air/5% CO_2 incubator at 37°C. The cells used in these experiments were passaged less than 5 times.

Collagen nanofiber scaffolds

The crimped fibril configuration (Figure 3.1A) is typical for collagen-based fibrous tissue not under an external load. There are two basic models of crimp collagen fibrils: planar wave/zig-zag model and cylindrical helix model[48] (Figure 3.1B), but neither of these can explain the double crimp pattern seen in Figure 3.1A. This structure is formed by combining the left-handed and right-handed helical fibrils into a double super helix structure. The fibrils nest together to create a crimp pattern that is formed by the bunching of adjacent fibrils. This model[49] is schematically represented in Figure 3.1C. The green fibrils are left-handed while the red fibrils are right-handed. The actual crimps are the cluster of peaks of the nested helices.
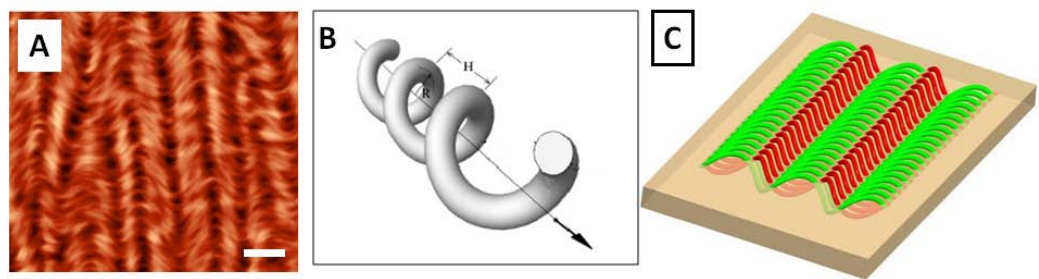
Figure 3.1: (A) AFM image of double crimp collagen matrix structure. (B) Cylindrical helix model of crimped collagen fibril, where R is the radius and H is the pitch of the helix. (C) Model of collagen structure with double crimp pattern. Left-handed and right-handed fibrils are shown in green and red, respectively. Scale bar represents 2 μm.

The collagen nanofiber scaffolds with the double super helix model described above were fabricated accordingly to previously published protocols.[50,51] The production process is based on technology developed for liquid crystal display (LCD) manufacturing [52,53,54,55,56] and is suitable for lyotropic liquid crystal materials. Purified monomeric collagen solution (bovine type I, 3 mg/ml) was purchased from Advanced BioMatrix (San Diego, CA, USA). This material was concentrated to reach a liquid crystal state and sheared onto glass with optical precision using a liquid film applicator assembly.[57] A second generation machine using air-bearing systems (Figures 3.2A, 3.2B) provides optimal conditions for the self-assembly of collagen molecules into aligned and aligned-braided fibrils. The glass substrate is mounted on a stage which is transported by a linear actuator under a stationary applicator head. The head was adjusted to produce collagen matrices of different coating thicknesses and required crimp structures with coating speeds of 100 mm/sec using small quantities (1-2 ml) of collagen solution at typical concentrations of 25 mg/ml. A representative image of the scaffold with 300 nm aligned collagen fibrils (300A) is shown in Figure 3.2C. Fiber diameter and alignment were varied by changing pH, collagen concentration, humidity and other factors.
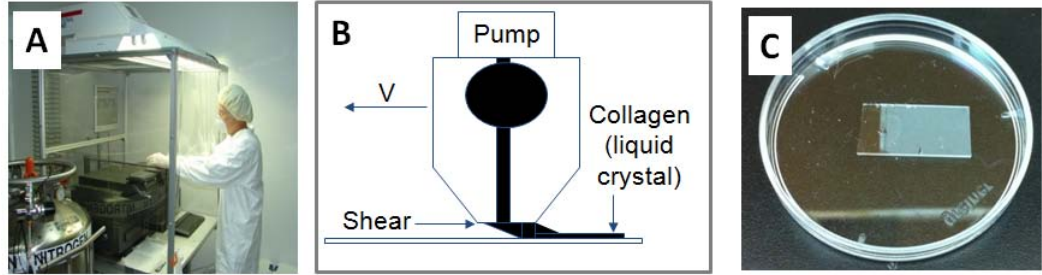
Figure 3.2: (A) Liquid film applicator assembly used for the fabrication of collagen nanofiber substrates. (B) Schematic representation of the applicator moving at variable coating speed, V, to dispense collagen in the liquid crystal form to produce fibrils. (C) Glass substrate fabricated with 300 nm parallel collagen fibrils, 300A.

For the fabrication of the unstructured collagen coated slides, flat glass substrates were rinsed in PBS and deionized water and then sterilized in 70% ethanol and covered with bovine collagen I (BD Biosciences) at a concentration of 50 μg/ml in 0.01 M HCl using a pipette and incubated at room temperature for one hour. Excess collagen solution was then aspirated and the slides were rinsed with PBS. Substrates were either used immediately or stored in 70% ethanol at 2 – 8 ℃ for up to two weeks before use.

Atomic force microscopy and diffraction

Samples were air dried before imaging using atomic force microscopy (AFM). The structure of the collagen fibrils on the glass substrate was observed using AFM Ntegra Prima and Solver Next (NT-MDT, Moscow, Russia). Images were acquired in the semi-contact mode using silicon tips NSG01 with typical radius < 10 nm and spring constant 5.1 N/m (K-Tek Nanotechnology, Wilsonville, OR, USA). The diffraction patterns were produced using a red (630nm) laser beam focused to a diameter of about 0.3 mm on the collagen layers deposited on glass substrates.

Visible light transmission

The transmission of visible polarized light through the 30A collagen layer was measured using a LAMBDA 950 UV/Vis/NIT Spectrophotometer (Waltham, Massachusetts, USA). Spectra were measured through the substrate and bare glass was used as the baseline which was then subtracted to obtain transmittance through the collagen layer alone. S-direction was parallel to the crimp and p-direction was parallel to the direction of the fibrils.

Confocal microscopy

Collagen nanofiber substrates (30A, 300A and 30NA) and collagen coated flat glass controls (FC) were seeded with corneal fibroblasts at a density of 10,000 cells/cm^2 in complete media and allowed to grow for two days. Complete media was changed to media without FBS the day after seeding. After two days, the cells were fixed in 4% paraformaldehyde (Fisher Scientific, Pittsburgh, PA, USA) for 15 min, permeabilized with 0.5% Triton X-100 (Sigma, St. Louis, MO, USA) for 5 min, and blocked with 1% bovine serum albumin (Sigma) for 30 min. F-actin was stained using Alexa Fluor 568 phalloidin (Invitrogen, Carlsbad, CA, USA) for 60 min. Nuclei were then counterstained with Hoechst 33258 for 5 min. All images were acquired using a Nikon C1si spectral confocal microscope.

Morphometric analysis

Cell shape index (CSI) is defined here as the dimensionless ratio: $4\pi * A * P^{-2}$, where A = cell area and P = cell perimeter.[58] CSI provides a measure of cell circularity with circular cells having values closer to one, and elongated cells having values

27

approaching zero. CSI was calculated from the spectral confocal images. Four images were acquired per substrate to calculate CSI values.

Quantitative polymerase chain reaction

Bovine corneal fibroblasts were seeded on the collagen nanofiber scaffolds – 30A, 300A, 30NA and FC at a density of 10,000 cells/cm^2. Complete media was changed to media without FBS the day after seeding. Samples were harvested after two days using the Ambion/Applied Biosystems's Cell to C$_T$ kit (Foster City, CA, USA). Lysis, RT-PCR, and qPCR were performed according to manufacturer's instructions using a StepOne Plus instrument (Applied Biosystems). The qPCR amplification protocol consisted of one cycle at 95 °C for 20 s followed by 40 cycles at 95°C for 3 s and 60°C for 30 s. The relative amount of cDNA was normalized to the amount of glyceraldehyde 3-phosphate dehydrogenase (GAPDH) present in each sample. Primers (Integrated DNA Technologies, Coralville, IA, USA) are provided in Table 3.1. Melt curve analyses was performed at the end of all PCRs to ensure the specificity of PCR. Each experimental condition was performed three to five times. Expression levels of the genes were measured in technical triplicates.

Statistical analysis

Statistically significant differences were estimated using analysis of variance (ANOVA) tests. For group differences shown to be significant by ANOVA, sequential Holm t-tests were performed to detect differences between specific pairs of substrates. Differences were considered significant if $p < 0.05$.

Gene	Primer sequence (5'–3')
COL1	F: CAACCATGCCTCTCAGAA CA R: GCCAGTTTCCTCATCCATGT
COL3	F: GTCCTGATGGTTCCCGTAAA R: TTCAGGATGGCAGAATTTCA
Fibronectin	F: TTGATCGCCCTAAAGGACTG R: CATCCTCAGGGCTCGAGTAG
Biglycan	F: TCTCAGAGGCCAAGCTCACT R: TAGCTCGAT TGCCTGGATTT
TKT	F: GACGGGCCCTCCCAGAT, R: CATCACTTGGGTAAAAGACAGTTGA
SMA	F: TGACCGCATGCAGAAGGA R: GGGCGATGATCTTGATCTTCA
GAPDH	F:GCATCGTGGAGGGACTTATGA R: GGGCCATCCACAGTCTTCTG

Table 3.1: Quantitative Polymerase Chain Reaction Primers

3.3 Results and Discussion

Characterization of nanofiber substrates

Collagen nanofiber scaffolds with the three different arrangements of collagen fibrils deposited on glass substrates (30A, 300A and 30NA) were fabricated by Fibralign Corporation. AFM analysis of the 30A substrate, mimicking native corneal fibrils, shows

highly aligned 30 nm collagen fibrils (Figure 3.3A). The direction of crimp is also shown (green arrow). AFM imaging of 300A substrates showed thick aligned fibrils with a diameter of around 300 nm (Figure 3.3B), while the 30NA substrates showed nonaligned fibrils with a diameter of approximately 30 nm (Figure 3.3C). All samples were uniformly covered with the collagen fibrils. Fibril arrangement remains intact after seeding cells as shown by scanning electron microscopy (Figure S3.2).
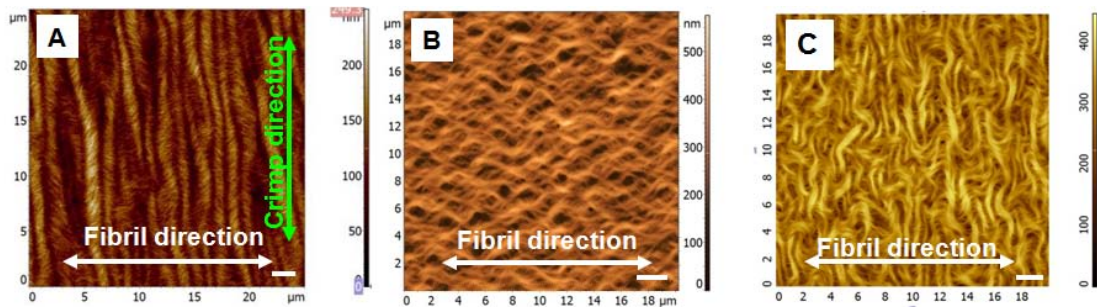
Figure 3.3: AFM images of the varying collagen fibril arrangements on glass substrates (A) 30 nm aligned—30A, (B) 300 nm or larger aligned—300A, and (C) 30 nm nonaligned—30NA, respectively. Scale bars represent 2 μm.

Diffraction patterns produced using a 630 nm laser beam were also used to assess the alignment of the fibrils. The two vertical petals and "cross" seen in the diffraction patterns in Figure 3.4A and 3.4B indicate a high alignment of the collagen fibrils on the 30A and 300A substrates. The elliptical diffraction area and high level of diffusive scattering in Figure 3.4C indicate a lesser alignment and poor periodicity of the crimp structure on the 30NA substrate.

The 30A substrate which mimics the fibril arrangement *in vivo* was further evaluated to measure the transmission of visible polarized light through the collagen layer. As seen in Figure 3.4D, the optical transmission through the collagen layer is high (~90%) in the visible region of the spectrum. The birefringence of the layer is consistent

with the form birefringence which is related to the aligned fibrillar structure of the 30A substrate. The high optical transmission through the 30A substrate should be beneficial for the use of these collagen films as templates for corneal tissue engineering scaffolds in future studies.
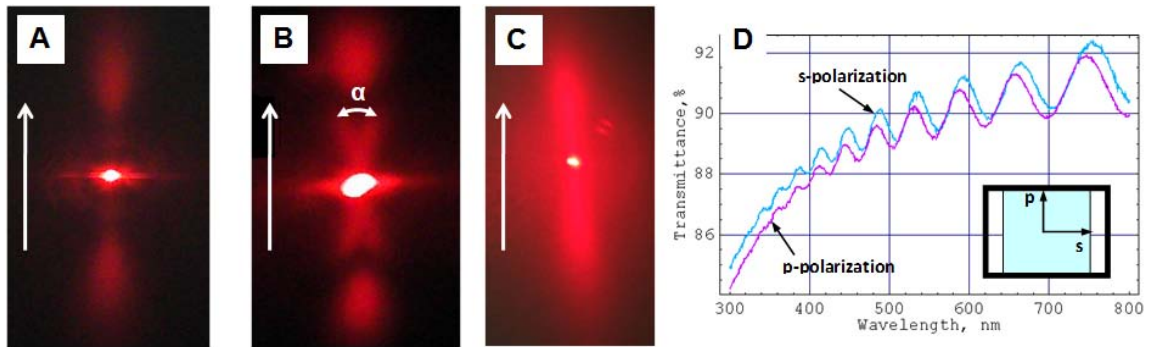
Figure 3.4: Diffraction patterns produced by red (630 nm) laser beam on the three collagen nanofiber substrates—(A) 30A, (B) 300A, and (C) 30NA, respectively. The two vertical petals in (A) indicate the uniform alignment of collagen fibrils on these substrates. The angle α of the crosslike area in (B) depends on fibril radius, R, and pitch of the helix, H. The elliptical shaped diffraction area and high level of diffusive scattering in (C) are indicative of the partial fibril alignment and poor periodicity of the crimp structure on this substrate. Arrows indicate fibril direction on each substrate. (D) Transmittance of visible polarized light thought the 30A collagen layer, where s-direction is parallel to the crimp and p-direction is parallel to the direction of the fibrils.

Corneal fibroblast morphology on collagen nanofiber substrates

To determine how matrix nanotopography affects cell morphology, bovine corneal fibroblasts were seeded on 30A, 300A and 30NA substrates and on the flat collagen coated control, FC. After two days, cells were fixed and stained with phalloidin to visualize the actin cytoskeleton and Hoechst to image the cell nucleus using confocal microscopy. Representative images are shown in Figure 3.5. Cells grown on the 30A substrate were highly aligned and exhibited elongated and dendritic morphologies, similar to those of corneal keratocytes which represent the quiescent phenotype (Figure 3.5A, 3.5E).[59] Multiple cells had extended processes interconnecting with other cells.

Cells on the 300A (Figure 3.5B, 3.5F) and 30NA (Figure 3.5C, 3.5G) were larger and more spread out with fewer processes extending out, while cells on the FC substrate were even more spread out with almost no extending processes as seen in Figure 3.5D and 3.5H. The cells that were spread out were similar in appearance to repair phenotypes such as fibroblasts and myofibroblasts[59] with filamentous actin forming stress fibers across the cell body.
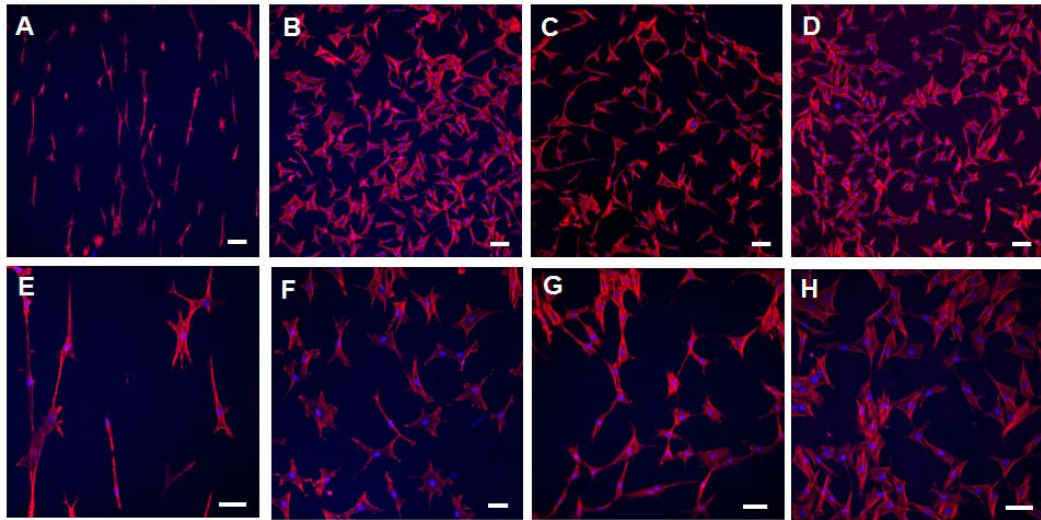
Figure 3.5: F-actin (phalloidin, in red) and nuclear (Hoechst, in blue) staining of corneal fibroblasts grown on (A) 30A, (B) 300A, (C) 30NA, and (D) FC substrates, respectively, (E), (F), (G), and (H) are the corresponding images shown at higher magnification. Scale bars represent 100 μm.

Morphometric analysis of the images obtained using confocal microscopy shows that there were significantly larger numbers of elongated cells on the nanofiber scaffolds (30A, 300A and 30NA) compared to the flat control, FC (Figure 3.6, *p<0.001). Also, the 30A substrate has the maximum number of elongated cells significantly higher than those on any of the other substrates as seen in Figure 3.6 (Δp<0.001). Thus corneal fibroblasts respond to the presence of the 30 nm, aligned collagen fibrils (30A) similar to

those seen *in vivo*, by reverting to the stellate morphology exhibited by corneal keratocytes.
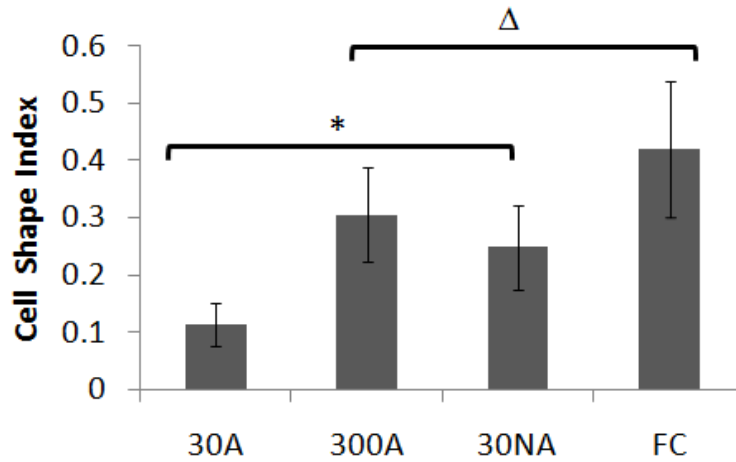
Figure 3.6: Cell shape indices of corneal fibroblasts grown on the nanofiber substrates (30A, 300A, and 30NA) and control (FC). Cells grown on 30A substrates have the lowest CSI and hence the most elongated morphology, while cells grown on controls (FC) have the largest CSI and hence assume a more spread-out morphology. *p < 0.001 vs. FC. Δp < 0.001 vs. 30A.

Previous studies with rabbit corneal fibroblasts have shown that the cells align themselves only on aligned collagen scaffolds and not on unaligned scaffolds or TCPS[37] in accordance with our results. Human corneal keratocytes cultured on micropatterned collagen also aligned along the direction of the grooves and secreted matrix proteins such as collagen 1 and keratan sulfate which appeared to be similarly aligned with the patterns.[45] In another study, rabbit corneal fibroblasts were seeded on collagen coated patterned polyurethane substrates. It was shown that cells align themselves strongly on pitch sizes of 800 nm or larger and not on feature sizes of 400 nm.[44] This is in agreement with our data, where cells do not align on collagen fibrils 300 nm or larger in diameter (300A). However, it is interesting to note that corneal fibroblasts respond to topography again when the feature size is further reduced to the 30 nm, aligned fibril arrangement similar to that seen *in vivo*. The corneal stroma is composed of collagen fibrils 30 – 35

nm in diameter, which are further arranged in orthogonal stacks called lamellae, which are 1 – 2 μm in thickness.[36] Thus the fact that the cells are able to respond to features on the order of microns (1 μm or larger, similar to lamellae), as well as down to nanometers (30 nm, similar to individual fibrils), could likely be influenced by the topography of the stromal fibrils and lamellae that the cells contact *in vivo*.

Target gene expression on collagen nanofiber substrates – 30A

Cell response was evaluated by qPCR for the following six markers – TKT, SMA, COL1, COL3, FN and biglycan. TKT is a corneal crystallin whose expression levels are elevated in the keratocyte phenotype[42] and SMA is a marker for the fibrotic myofibroblast phenotype.[59] COL1, COL3, FN and biglycan are matrix proteins in the corneal stroma, all of which are up-regulated during scar formation.[59] We hypothesized that 30A substrates which mimic matrix topography *in vivo*, provide cues that decrease fibrosis and promote regeneration in corneal fibroblast cultures. As seen in Figure 3.7, qPCR analysis revealed a significant change in expression levels of TKT and SMA on 30A substrates compared to the flat controls, FC. When normalized by TKT expression on FC, corneal fibroblasts on 30A expressed 1.94 ± 0.51 times that of TKT levels on FC ($p<0.05$). qPCR also showed a two-fold decrease in SMA expression on the 30A compared to FC. When normalized by expression on FC, SMA expression was 0.49 ± 0.11 fold decreased on 30A ($p<0.05$).

Healthy corneal keratocytes are associated with abundant levels of TKT expression, and almost no expression of SMA.[41,42] Thus it is seen that the presence of 30 nm, aligned collagen fibrils provides cues that promote the formation of the quiescent keratocyte phenotype by reducing SMA expression and increasing levels of TKT, which in turn, contributes to cellular transparency in the cornea. This data is in excellent agreement with our fluorescence microscopy results showing that maximal numbers of

corneal fibroblasts assume an elongated, dendritic morphology resembling that of keratocytes on the 30A substrates compared to FC controls. Similar studies using rabbit corneal fibroblasts have shown that the percentage of fibroblasts expressing SMA is significantly reduced on scaffolds containing aligned collagen fibers when compared to cells grown on TCPS over a two-week period.[37] Our study shows that this effect is seen as early as two days, and is accompanied by an increase in TKT gene expression. Previously it has been shown that poly(ethylene glycol) dimethacrylate hydrogel microrods in three-dimensional scaffolds significantly down-regulated SMA expression in 3T3 mouse fibroblasts, showing that topographical cues attenuate the expression of the fibrotic phenotype similar to our results.[60]
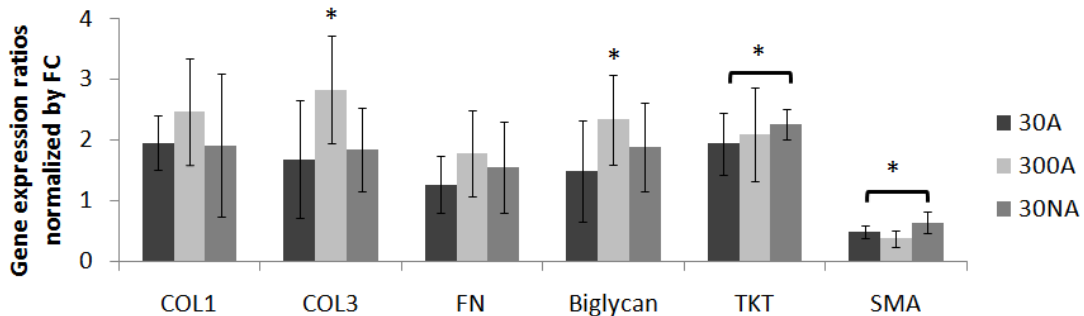
Figure 3.7: qPCR analysis of expression of matrix proteins (COL1, COL3, FN, and biglycan) and markers (TKT and SMA) in corneal fibroblasts grown on 30A, 300A, and 30NA substrates normalized by expression levels of the same gene targets in cells grown on FC controls. All experiments were performed using cells at P3 or P4. GAPDH served as endogenous control. Data is presented as average ± standard deviation. Three to five replicates were used for each substrate. $*p < 0.05$ vs. FC.

While corneal fibroblast phenotype seemed to be sensitive to topography, COL1, COL3, FN and biglycan mRNA transcript levels on the 30A substrates were all statistically similar to FC controls (Figure 3.7). This suggests that matrix synthesis is not affected by the presence of 30 nm, aligned collagen fibrils. It has been shown that

collagen synthesis in the corneal stroma is dependent on MEK kinase 1 (MEKK1), a member of the mitogen-activated protein kinase (MAPK) family.[61] Similarly, transforming growth factor-beta (TGF-β) mediated fibronectin synthesis occurs through a c-Jun N-terminal kinase dependent, Smad independent pathway in corneal stromal cells, while SMA expression requires signaling through Smad3.[41,62] This could possibly explain why the effect of topography on the synthesis of matrix proteins such as fibronectin could be uncoupled from phenotype markers such as SMA.

Target gene expression on collagen nanofiber substrates – 300A

Fibril diameter is increased in scarred corneal tissue[63] leading to increased light scattering and loss of transparency. In order to examine the relative contribution of large fibril diameter on cell phenotype and matrix production, corneal fibroblasts were cultured on aligned collagen fibrils, 300 nm or larger in diameter (300A). Cell response was evaluated by qPCR analysis of the six targets listed above and mRNA expression was normalized to that of FC controls (Figure 3.7). Similar to the 30A substrates, TKT levels were increased and SMA levels were decreased on 300A substrates compared to FC. TKT expression on 300A substrates was 2.10 ± 0.78 times that of FC ($p<0.05$), while SMA expression was 0.38 ± 0.13 times that of FC, when normalized to FC ($p<0.05$). This suggests that fibril alignment has an effect on phenotype even at large diameters, as large fibrils when aligned, still promote the keratocyte phenotype (high TKT) and down-regulate the fibrotic phenotype (low SMA). This data is also in agreement with our fluorescence microscopy data which shows that there are more numbers of elongated cells (which resemble the keratocyte phenotype) on 300A substrates compared to FC controls.

However unlike the 30A scaffolds, qPCR analysis shows that COL3 and biglycan mRNA transcript levels were both significantly up-regulated in the presence of large fibrils when compared to flat controls (FC). COL3 expression was 2.83 ± 0.69 ($p < 0.05$) and biglycan expression was 2.34 ± 0.73 ($p < 0.05$) times respectively, on 300A compared to FC, when each was normalized to FC substrates. COL1 and FN levels were also increased on 300A compared to FC (2.47 ± 0.62 times for COL1, and 1.79 ± 0.68 times for FN, respectively) although not to statistically significant levels. Thus matrix synthesis is up-regulated in the presence of large diameter fibrils. There was no significant difference in gene expression levels between the 30A and 300A substrates.

Collagen fibrils in the normal stroma are very weak in scattering light because their diameter is smaller than the wavelength of light leading to a highly transparent cornea.[36] Collagen fibril diameter is significantly increased in corneal wound[64] and scar tissues.[63] It has been suggested that the enlargement in fibril diameter is responsible for the increase in light scattering associated with the scar tissue.[63] The increased synthesis of matrix proteins associated with large diameter fibrils could possibly lead to disorganized deposition of the matrix, which could explain the high scattering and reduced transparency observed in scar tissue.

Target gene expression on collagen nanofiber substrates – 30NA

Following injury, collagen fibrils in these regions of the cornea lose their highly ordered arrangement. Over time, the fibrils regain their alignment thus suggesting that aligned fibrils are important for proper wound repair.[65] Accordingly, corneal fibroblasts were cultured on 30 nm nonaligned collagen fibrils to examine the relative contribution of fibril alignment on cell phenotype and matrix production. Cell response was evaluated

by qPCR analysis of the markers and matrix proteins listed above. As seen in Figure 3.7, TKT expression was significantly increased and SMA expression was significantly down-regulated on 30NA substrates compared to FC, similar to the results with the other two nanofiber scaffolds. TKT levels on 30NA substrates were 2.26 ± 0.26 times that of FC ($p<0.05$), while SMA expression levels were 0.64 ± 0.18 times that of FC ($p<0.05$). This suggests that cells still respond to collagen fibrils at the optimal diameter of 30 nm by up-regulation of the quiescent phenotype (high TKT) and down-regulating the repair phenotype (low SMA) even in the absence of complete alignment. This data is in accordance with our confocal microscopy data which shows that there are more numbers of elongated cells (similar to the keratocyte phenotype) on 30NA substrates compared to FC controls. As with the 30A substrates, mRNA transcript levels of all the matrix proteins tested - COL1, COL3, FN and biglycan, were statistically similar to that of the FC control. This suggests that matrix synthesis is not affected by the nonalignment of 30 nm collagen fibrils. Gene expression levels on the 30NA substrates were statistically similar to those on 30A substrates.

Previously it has been shown that there is a reduction in the expression of SMA in rabbit corneal fibroblasts grown on aligned collagen fibers compared to cells grown on unaligned collagen substrates.[37] This difference could be due to the fact that these cells were cultured for a seven day period in media containing FBS, which is an activator of the repair fibroblast phenotype.[47] In our study however, complete media was changed to media without FBS after day one, and cells were harvested on day two for qPCR analysis. The longer exposure time to FBS could possibly amplify the differences in

response between cells grown on collagen fibers without and without complete alignment leading to a difference in results between the two studies.

It has long been thought that the presence of monodisperse and aligned fibrils with regular ordered arrangement is required for a transparent cornea.[66] However, it has been shown that disordered collagen fibrils can still be transparent as long as they do not contain regions of collagen larger than the wavelength of light.[67,68] These results are in accordance with our data which shows that at the optimal diameter of 30 nm, there is no difference in target gene expression between aligned and nonaligned fibrils.

Conclusion

This study shows that environmental cues such as collagen fibril diameter and alignment may be used to promote the transformation of corneal fibroblasts from the repair phenotype (fibroblasts and myofibroblasts) towards the quiescent phenotype (keratocytes). Our fabrication process allows for self-assembly of molecular collagen into fibrils with control of fibril diameter and alignment. This process is able to deposit highly uniform, transparent collagen scaffolds. Although previous studies have looked at corneal fibroblast alignment, migration[44] and SMA expression[37] in response to topography, the expression of corneal crystallins and matrix proteins which play a major role in corneal wound healing has not been investigated. Our study evaluates gene expression levels of the myofibroblast marker SMA, the corneal crystallin, TKT, and matrix proteins such as collagens 1 and 3, fibronectin and biglycan, in response to collagen fibril topography. Furthermore, we have examined the effect of both fibril diameter and alignment on cell morphology and gene expression. Our results show that the expression of SMA is down-

regulated, while TKT expression is increased on all three nanofiber scaffolds (30A, 300A and 30NA) compared to flat collagen coated controls. This suggests that the presence of collagen fibrils attenuates the fibrotic phenotype and promotes expression of the quiescent phenotype, both of which are linked to an increase in cellular transparency in the cornea. Further, matrix synthesis is increased on the 300A substrates, which could be a possible reason for the increased light scattering and loss of transparency observed in scar tissue associated with large diameter fibrils. Our finding that fibril diameter and alignment can affect myofibroblast differentiation, keratocyte regeneration and matrix synthesis suggests that matrix topography may play an important role in corneal development, disease and repair after injury. Future studies that investigate cell response in three-dimensional collagen nanofiber scaffolds and explore the molecular mechanisms involved in the regulation of such responses could benefit the design of tissue engineered corneas and promote our understanding of corneal wound healing processes.

CHAPTER 4. Effect of collagen nanotopography on keloid scar healing

4.1 Background

Keloids are raised dermal scars which extend beyond the boundaries of the initial injury. They are unique to humans, with no good animal models available.[69] They are more common in dark skinned individuals and affect about 4 – 16% of the black and Hispanic population.[70] They are often incapacitating with intense pain and cause both functional and aesthetic problems in affected individuals. Keloid fibroblasts have a higher rate of proliferation, more excessive deposition of extracellular matrix (ECM) proteins such as collagens I and III, and increased expression of the myofibroblast marker, α-smooth muscle actin (SMA), compared to normal dermal fibroblasts.[71] The major drawback of current treatments such as surgical excision and intralesional steroid injections is the high rate of recurrence.[72] An effective therapy that prevents recurrence would greatly benefit keloid treatment.

The aggressive nature of a keloid is demonstrated by the fact that the center of the keloid is in clinical regression, and has a reduced rate of cell proliferation, while fibroblasts in the growing margin are highly proliferative and often invade the surrounding healthy tissue.[73,74] The organization of collagen fibers in a keloid is more parallel compared to that of normal skin.[75] Hence, at the center of the scar cells reside on a matrix of highly aligned collagen fibrils and show decreased proliferation; whereas at the active margin, cells encounter a random network of collagen fibrils as seen in normal skin, and exhibit high rates of proliferation. Not only is the rate of proliferation very different at the two regions of the keloid, but also there is a difference in collagen fibril organization, suggesting a correlation between collagen architecture and keloid growth.

Al-Attar *et al.* suggested that mechanical tension during wound healing results in the misalignment of collagen fibrils and causes the formation of aberrant scars such as keloids.[76] In addition, it has been shown that cryotherapy which induces a greater parallelization of collagen fibers is accompanied by a decrease in keloid scar volume.[77] Consequently, we hypothesize that the alignment of collagen fibrils might result in the reduction of keloid fibroblast proliferation and other associated abnormalities such as elevated collagen synthesis and SMA expression.

There is abundant evidence in literature indicating that topography affects cell proliferation and matrix synthesis. A previous study using aluminum oxide membranes showed that nanopore size influences keratinocyte proliferation and migration, both of which affect wound repair and reconstruction.[78] Another study using fibroblasts cultured on polymer microrods showed that microtopography affected cell proliferation and downregulated synthesis of matrix proteins involved in scar formation.[60] Additionally, previous work in our group using corneal fibroblasts cultured on collagen nanofiber substrates has shown that fibril diameter and alignment both promote the quiescent keratocyte phenotype and downregulate matrix synthesis.[79]

The objective of this study was to evaluate the effect of collagen fibril topography on keloid fibroblast proliferation, morphology and matrix synthesis, all of which are indicators of wound healing in the skin. To this end, we cultured human fibroblasts from the following types of tissue – normal skin (human dermal fibroblasts, HDF), normal scar (scar fibroblasts, SF) and keloid scar (keloid fibroblasts, KF) on four collagen nanofiber substrates similar to those used in our previous study.[79] The three cell types represent a spectrum of fibroblasts seen in dermal wound healing ranging from healthy (HDF) to

42

normal (SF) and abnormal wounds (KF), respectively. The four substrates selected for this study were glass slides coated with nanopatterned collagen films with the following fibril diameter and orientation – 30 nm aligned (30A), 30 nm random (30R), 200 nm aligned (200A) and 200 nm random (200R) fibrils, respectively. Human dermis is made up of randomly arranged collagen fibers 50 - 60 nm in diameter.[80] The 30A and 30R fibrils therefore, represent the collagen fiber arrangement seen in scar (both normal and keloid scar), and skin tissue, respectively. Further, it has been reported that collagen fiber diameter changes during the course of wound healing in the skin.[80] The 200A and 200R substrates were therefore selected to investigate the effect of change in fibril diameter on dermal wound healing. Collagen–coated glass substrates were used as flat controls (FC) with no predetermined topography.

Fibroblast morphology was visualized using confocal microscopy and cell proliferation was measured using the CyQuant assay. Quantitative polymerase chain reaction (qPCR) was performed on six targets related to proliferation (cyclin D1), phenotype (SMA) and matrix synthesis (collagens I and III, and matrix metalloproteinases – MMP-1 and MMP-2) to examine the effect of nanotopography at the level of gene expression. Understanding how matrix topography affects cell behavior and wound healing could aid in the design of an effective therapy for keloid scars.

4.2. Materials and Methods

Cell culture

KF and SF were a gift from Dr. Shirley Russell at Vanderbilt University. The fibroblast isolation and propagation procedures have been described elsewhere.[81,82] HDF

were obtained from Invitrogen (Grand Island, NY). All cells were cultured in complete medium consisting of Dulbecco's modified Eagle's medium with 10% fetal bovine serum (FBS) and 1% penicillin/streptomycin (Gibco, Grand Island, NY) in a humidity controlled incubator maintained at 37 °C and 5% CO_2. Collagen nanofiber scaffolds (30A, 30R, 200A and 200R) and FC controls were seeded with KF, SF and HDF at a density of 10,000 cells/cm^2 in complete medium. The complete medium was changed to serum-free medium 24 h after seeding, as FBS has been shown to act as an external wounding agent, [83,84] At the end of two days, cells were fixed or lysed for further studies. The cells used in these experiments were passaged less than five times.

Scaffold fabrication and characterization

The collagen nanofiber scaffolds were fabricated using a nanoweave technology developed by Fibralign Corporation (Sunnyvale, CA). The details of this process have been described earlier.[79] Briefly, bovine collagen I solution in the liquid crystal state was shear extruded onto a glass slide using a liquid film applicator. Collagen concentration, pH, humidity and other factors were varied to provide optimal conditions for the self-assembly of collagen into fibers of various diameters and orientations. Collagen scaffolds were rinsed in phosphate buffered saline (PBS) and deionized water, and sterilized with 70% ethanol before use in cell culture. To prepare the flat collagen-coated controls, glass slides were washed in PBS and deionized water, sterilized with 70% ethanol and dipped in bovine collagen I solution (50 µg/ml in 0.01 M HCl) at room temperature for one hour. Subsequently, slides were rinsed in PBS and used directly or stored in 70% ethanol at 2 – 8 ºC for up to two weeks before use. Scaffolds were air dried and imaged using atomic force microscopy (AFM) to measure fiber diameter and orientation. All experiments were

44

performed using the AFM Ntegra Prima and Solver Next (NT-MDT). AFM topographs were recorded using silicon tips NSG01 with typical radius < 10 nm and spring constant 5.1 N/m (K-Tek Nanotechnology) in the semi-contact mode.

Fluorescent microscopy

Substrates were fixed in 4% paraformaldehyde (Fisher Scientific, Pittsburgh, PA) for 15 minutes, then permeated with 0.5% Triton X-100 for five minutes, and blocked with 1% BSA (Sigma, St. Louis, MO) for 30 minutes. Finally, substrates were incubated with Alexa Fluor-568 conjugated phalloidin (Invitrogen, Grand Island, NY) at 1:100 dilution for 60 minutes followed by Hoechst 33258 (Invitrogen, Grand Island, NY) at 1:2000 dilution for five min. Samples were then visualized using confocal microscopy.

Proliferation Assay

Two days after seeding, cell proliferation was measured using the CyQuant assay (Life Technologies, Grand Island, NY). Fluorescence was measured at 480 nm excitation and 520 nm emission, and compared to a standard curve to determine proliferation rates for the different cell types on each scaffold. Three biological replicates were used for each cell type and the assay was performed in technical triplicates.

Quantitative Polymerase Chain Reaction

The RNAqueous-4PCR kit (Applied Biosystems, Grand Island, NY) was used for RNA extraction. The isolated RNA was reverse transcribed into complementary DNA (cDNA) using the Cells to C_T kit (Applied Biosystems, Grand Island, NY). Primers were obtained from Integrated DNA Technologies (Coralville, Iowa). qPCR was performed on the StepOne Plus using Fast SYBR Green PCR Master Mix. The cDNA obtained from

the target mRNA was normalized to that of glyceraldehyde 3-phosphate dehydrogenase (GAPDH). Three to five biological replicates were used per substrate. qPCR was performed in technical triplicates.

Statistical analysis

ANOVA was used to compare group means both between the nanofiber scaffolds and between the three cell types. Differences were considered significant at the $p < 0.05$ level. If a significant difference was seen by ANOVA, then sequential Holm t-tests were conducted to detect specific differences between scaffolds or between cell types.

4.3 Results and Discussion

Characterization of nanofiber substrates

AFM analysis of the 30A substrate revealed the presence of 30 nm aligned collagen fibrils representative of the collagen arrangement seen in both normal scar and keloid scar tissue (Figure 4.1).[75] AFM imaging of the 30R substrate showed randomly organized fibrils, 30 nm in diameter, representing the collagen arrangement in healthy skin.[80] AFM images of the 200A and 200R substrates showed thicker aligned and random fibrils, respectively, which were selected to investigate the effect of change in diameter on fibroblast proliferation and ECM production. The image of the collagen-coated flat glass slide, FC, shows the absence of any fibrils and represents the flat control used in our study.
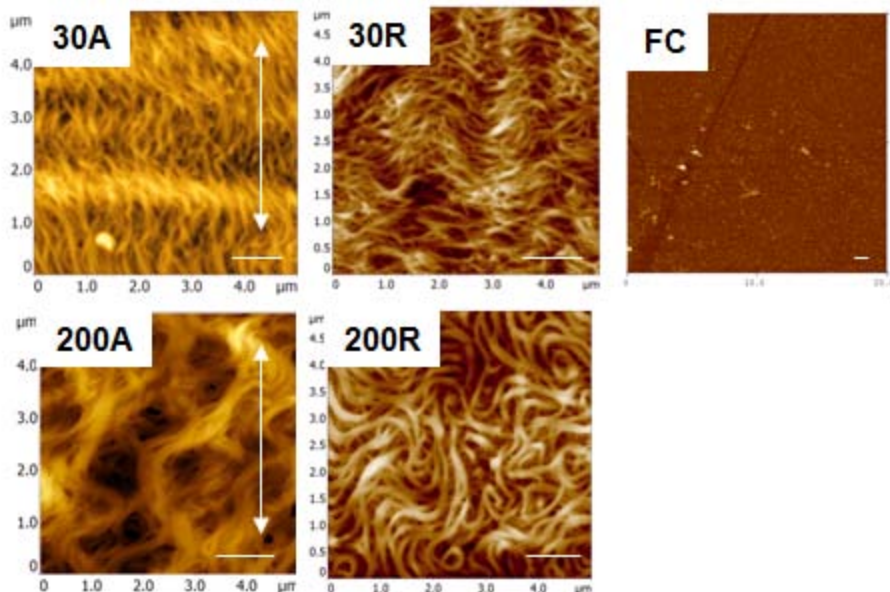
Figure 4.1: AFM images of the nanopatterned collagen substrates and flat control. The five images represent 30 nm aligned fibrils (30A), 30 nm random fibrils (30R), 200 nm aligned fibrils (200A), 200 nm random fibrils (200R), and flat collagen-coated control substrate (FC), respectively. Arrows represent fibril direction. Scale bars represent 1 μm.

Fibroblast adhesion and morphology on collagen nanofiber substrates

Previously, we have shown that fibril arrangement affects corneal fibroblast morphology and adhesion to nanopatterned collagen scaffolds.[79] To determine if this effect is also seen in fibroblasts related to dermal wound healing, KF, SF and HDF were grown on the nanostrusctured scaffolds and controls and stained to image f-actin (phalloidin) and the nucleus (Hoechst). As seen in Figure 4.2, fibroblasts on the 30A substrate exhibited a more dendritic and elongated morphology compared to cells on the other nanofiber substrates and FC control, which were larger, flatter and more spread out with the appearance of numerous stress fibers. Also, fewer fibroblasts appeared to adhere to the 30A substrates for all three cell types. Thus fibril alignment influenced cell

morphology and adhesion in all three cell types. Adhesion and spreading have been shown to be important for viability[85] and proliferation[86] of anchorage dependant cells such as fibroblasts. A previous study using keratinocytes grown on aluminum oxide nanoporous membranes also showed that greater cell spreading correlated with higher levels of proliferation.[78] Therefore we hypothesized that decreased cell attachment and spreading will lead to lower proliferation on the 30A samples compared to the other substrates in the study.
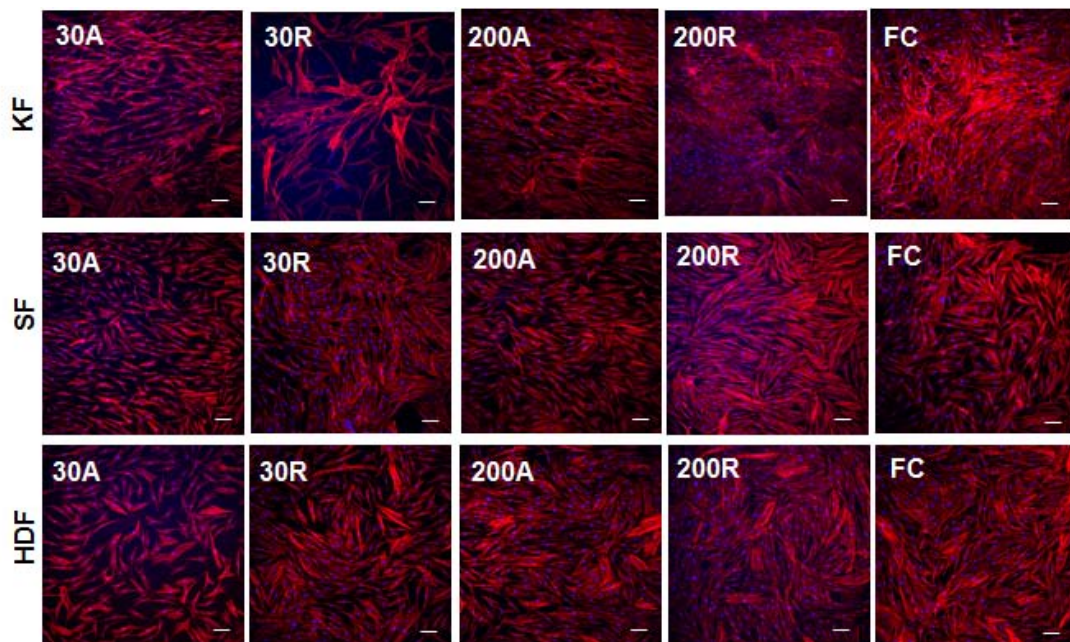
Figure 4.2: Confocal microscopy images of fibroblasts on collagen nanofiber substrates and flat controls. F-actin (phalloidin) is shown in red and the nucleus (Hoechst) is shown in blue. Scale bars represent 100 μm.

Collagen nanotopography reduces fibroblast proliferation

Excessive proliferation is a hallmark of keloid scars.[87,88] To determine the effect of collagen nanotopography on proliferation, fibroblasts proliferation was measured using the CyQuant assay. As seen in Figure 4.3, fibril alignment reduced KF proliferation (0.51

± 0.35 fold on the 30A substrate and 0.65 ± 0.19 on the 200A substrate, relative to FC, $p<$ 0.05 in each case). Fibril alignment (30A) also downregulated SF proliferation (0.49 ± 0.15 on 30A compared to FC, $p<0.05$). Fibril alignment (30A) reduced HDF proliferation as well (0.62 ± 0.31 on 30A compared to FC), although not to statistically significant levels. Therefore, fibril alignment (30A) showed a tendency to reduce proliferation of all three types of fibroblasts. These results are in accordance with our fluorescent microscopy data which showed that the 30A substrate had reduced cell adhesion and spreading, both of which are linked to decreased proliferation.[85,86]
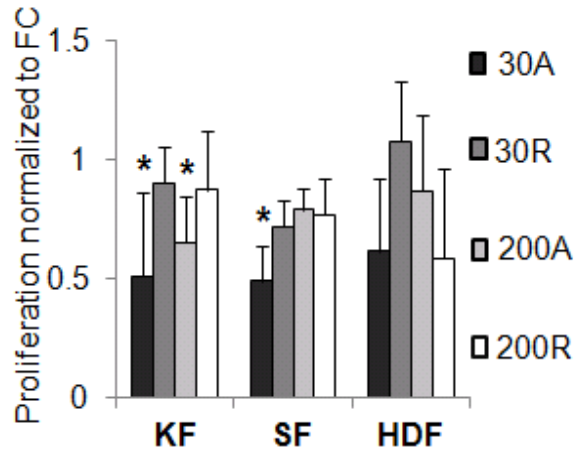
Figure 4.3: Fibril alignment (30A) reduced cell proliferation for KF, SF and HDF as shown by CyQuant assay. Data is presented as mean ± SD, using three replicates per substrate. * $p<0.05$ vs. corresponding values in the FC control of each cell type.

Additionally, fibroblasts from scar tissue (both keloid and normal scar) seem to be more responsive to collagen nanotopography compared to fibroblasts from normal skin. Previous studies have reported that KF are more responsive to serum stimulation[71] and show increased DNA and collagen production in response to TGF-β.[89] It has been speculated that increased expression and phosphorylation of signal transducer and

activator of transcription 3 (STAT-3), due to induction by cytokines and growth factors in KF, could possibly explain their enhanced response to chemical cues such as serum and TGF-β.[71] Here we have shown that KF also show increased sensitivity to physical cues such as matrix topography. To understand the mechanism underlying this response, we performed qPCR on six genes involved in fibroblast proliferation, phenotype expression and ECM synthesis, all of which are markers of keloid wound healing.

Collagen nanotopography reduces Cyclin D1 expression

It has been suggested that the increase in KF proliferation is due to their lower barrier for entry into S phase.[87] Cyclin D1 is a protein that forms complexes with cyclin-dependent kinase and acts as a switch regulating entry of cells into S phase.[90] Hence expression of cyclin D1 mRNA was measured to investigate its role in fibroblast response to topography. As seen in Figure 4.4a, cyclin D1 expression in KF was significantly reduced on three of the four nanostructured scaffolds as compared to FC (0.65 ± 0.29 on 30A, 0.41 ± 0.20 on 30R, and 0.36 ± 0.21 on 200A, compared to FC respectively, $p<0.05$ in each case). Cyclin D1 levels were also reduced on 200R, although not to statistical significance. This indicates that the presence of collagen fibrils, regardless of their arrangement, affects cyclin D1 gene expression in KF.

In SF, cyclin D1 expression was significantly reduced on 30A alone (0.58 ± 0.21 compared to FC, $p<0.05$). This corresponds very well with the results of the CyQuant assay where SF proliferation is downregulated only on 30A (Figure 4.3). The trend in cyclin D1 expression in SF on the other scaffolds also correlates to their proliferation profiles as seen with the CyQuant assay. In the case of HDF, cyclin D1 levels were reduced on all of the nanopatterned substrates compared to FC, similar to KF. This

difference reaches statistical significance for 30R and 200A (0.47 ± 0.31 for 30R and 0.40 ± 0.18 for 200A, compared to FC, $p<0.05$) (Figure 4.4a). Also, cyclin D1 levels were significantly downregulated in KF compared to SF for the 30R and 200A samples, respectively ($p<0.05$) (Figure 4.4a). In summary, 30A is most effective in reducing cyclin D1 levels across all three cell types and KF seem to be more sensitive to the effect of collagen nanotopography compared to SF, with respect to cyclin D1 expression.
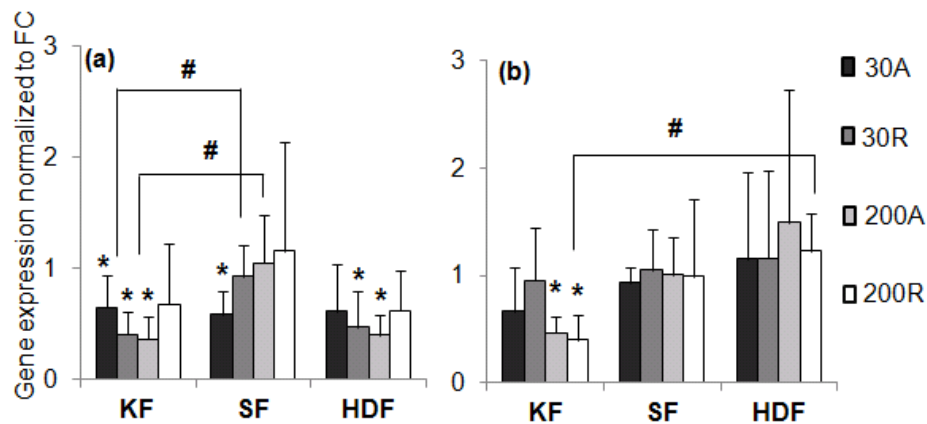
Figure 4.4: Fibril alignment (30A) reduced gene expression of (a) cyclin D1 and (b) SMA most effectively in KF. Data is presented as mean $\pm$ SD, using three to five replicates per substrate. *$p<0.05$ vs. corresponding values in the FC control of each cell type. #$p<0.05$ vs. corresponding values in KF.

Collagen nanotopography attenuates the fibrotic myofibroblast phenotype

SMA is an established marker of the myofibroblast phenotype and its expression is reported to be increased in KF.[91] As shown in Figure 4.2, fibroblasts on 30A substrates display an elongated morphology, while fibroblasts on other substrates were spread out with more prominent appearance of stress fibers, indicative of the myofibroblast phenotype. Hence SMA gene expression was measured to determine the effect of nanotopography on phenotype. SMA expression in KF was decreased on 30A, 200A and

200R compared to FC (Figure 4.4b). The decrease was statistically significant for 200A and 200R (0.47 ± 0.15 and 0.40 ± 0.23 compared to FC respectively, $p<0.05$). Therefore SMA expression in KF is decreased in the presence of collagen fibrils, similar to the expression of cyclin D1. This decrease was however not seen in the case of SF or HDF, thus suggesting that KF are more responsive to nanotopography with respect to SMA gene expression. Furthermore, SMA levels on the 200R substrate in KF were more significantly reduced compared to corresponding values in HDF ($p<0.05$).

Collagen nanotopography reduces matrix synthesis

Excessive collagen accumulation is a histological characteristic of keloid scars. This is due to both excessive collagen synthesis[92,93] and abnormal collagen turnover by matrix metalloproteinases such as MMP-1 and MMP-2.[84] Cells from the active margin of keloid scars have been shown to have increased expression of collagen I and III mRNA.[93]. Additionally, the levels of MMP-1, an interstitial collagenase, and MMP-2, which breaks down denatured collagens, are elevated in KF compared to HDF.[84] It has been suggested that MMP-1 and MMP-2 may be involved in KF migration, and therefore their increased production contributes to the invasive growth of keloid scar into the surrounding healthy skin. Hence, we measured the gene expression of collagens I and III, and MMP-1 and MMP-2, to determine the effect of nanotopography on ECM accumulation.

As seen in Figure 4.5a, collagen I gene expression in KF was significantly downregulated on all four nanofiber scaffolds compared to FC (0.46 ± 0.23 on 30A, 0.22 ± 0.21 on 30R, 0.28 ± 0.04 on 200A, and 0.31 ± 0.20 on 200R, as compared to FC, respectively, $p< 0.05$ in each case). Thus the presence of collagen fibrils, regardless of

their diameter or orientation, decreases collagen I expression in KF, following the trend seen with cyclin D1. In the case of both SF and HDF, collagen I gene expression was reduced only on the 30A substrate, with SF showing statistically significant reduction (0.48 ± 0.14 on 30A compared to FC, $p < 0.05$). Also, the decrease in collagen I expression in KF is greater compared to corresponding values in HDF for both 30R and 200R, respectively ($p < 0.05$). A similar trend was observed with collagen III wherein 30A is the only scaffold to show reduced collagen III expression across all the three cell types compared to FC (Figure 4.5b). Furthermore, this reduction is statistically significant only in KF (0.63 ± 0.09 on 30A compared to FC, $p < 0.05$). In summary, 30A scaffold is most effective in reducing expression of both collagens I and III across all three cell types. Also, KF are more responsive to nanotopography compared to SF and HDF.
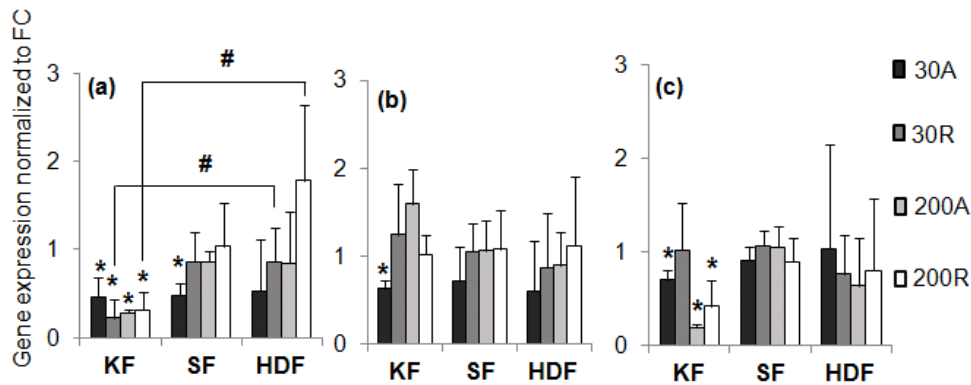
Figure 4.5: Fibril alignment (30A) reduced matrix synthesis most effectively in KF. Target gene expression of collagen I, collagen III and MMP-2 are shown in (a), (b) and (c), respectively. Data is presented as mean $\pm$ SD, using three to five replicates per substrate. *$p < 0.05$ vs. corresponding values in the FC control of each cell type. #$p < 0.05$ vs. corresponding values in KF.

Expression of MMP-1 in KF was slightly decreased on the nanofiber scaffolds compared to FC, although not to statistically significant levels (Figure S4.1). However, the same trend is seen as with most of the other markers, wherein KF are more responsive

to nanotopography as there was no decrease in MMP-1 expression with both SF and HDF, respectively. On the other hand, MMP-2 levels in KF were significantly reduced on three of the four nanofiber scaffolds – 0.70 ± 0.11 on 30A, 0.20 ± 0.03 on 200A, and 0.42 ± 0.28 on 200R compared to FC, respectively ($p<0.05$ in each case) (Figure 4.5c). The difference in KF response between MMP-1 and MMP-2 suggests that nanotopography acts differently on the different members of the MMP family. Interestingly, immunohistochemistry on keloid tissue showed higher expression of MMP-2 and not that of MMP-1, when compared to healthy skin controls,[94] indicating that MMP expression in keloids is also altered *in vivo*. Additionally, there was no change in MMP-2 expression on the nanopatterned substrates for both SF and HDF, showing that nanotopography modulates MMP-2 expression only in the case of KF, similar to the trend seen with some of the other proteins (SMA, collagen III and MMP-1).

Table 4.1 summarizes the effect of collagen fibril diameter and alignment on the three cell types used in the study. Overall, we observed that fibril alignment (30A and 200A) reduced cell proliferation and expression of genes related to proliferation (cyclin D1), fibrotic phenotype (SMA), and ECM synthesis (collagen I and III and MMP-2), respectively. Further, KF showed enhanced responsiveness to the effects of nanotopography. This is very desirable from a therapeutic standpoint to control keloid proliferation and inhibit scar growth, while still allowing for dermal fibroblasts to repopulate the region and complete wound healing. Future work will focus on fabrication of stand-alone collagen nanofiber films for use as a dermal patch in keloid treatment. A collagen patch would be fully biocompatible, biodegradable, non-invasive and have minimal side effects compared to the current standard of care (surgical excision or

intralesional steroid injections). Further studies exploring the molecular mechanisms involved in cell response will also aid the design of an effective approach for keloid management.

		Aligned fibrils				Random fibrils		
		KF	SF	HDF		KF	SF	HDF
30 nm fibrils	**30A**				**30R**			
	Proliferation	↓	↓		Proliferation			
	Cyclin D1	↓	↓		Cyclin D1	↓		↓
	SMA				SMA			
	Collagen I	↓	↓		Collagen I	↓		
	Collagen III	↓			Collagen III			
	MMP2	↓			MMP2			
200 nm fibrils	**200A**				**200R**			
	Proliferation	↓			Proliferation			
	Cyclin D1	↓		↓	Cyclin D1			
	SMA	↓			SMA	↓		
	Collagen I	↓			Collagen I	↓		
	Collagen III				Collagen III			
	MMP2	↓			MMP2	↓		

Table 4.1: Fibril alignment reduced proliferation and target gene expression most effectively in KF. Downward arrows indicate statistical significance compared to corresponding FC values ($p < 0.05$).

CHAPTER 5. Conclusions and Future Directions

In this work, we have examined the hemocompatibility and anti-fibrotic properties of two types of materials. The first was a set of biocompatible polymers which were used to modify the surface of silicon substrates for use in renal implant systems. The unmodified silicon substrates displayed low coagulation and complement activation; however, they had high levels of platelet adhesion and activation, both of which are detrimental for blood compatibility. Surface modification of the silicon samples showed the tendency to reduce platelet attachment and activation which would result in improved hemocompatibility of the silicon substrates for their use in implantable devices.

The second material under study was collagen, a biopolymer found in the extracellular matrix of cells. The nanoscale topography of collagen fibrils was manipulated to mimic the arrangement seen in different tissues such as cornea and skin to study cell response to topography. The corneal stroma is composed of aligned collagen fibrils, 30 nm in diameter. It was hypothesized that both fibril alignment and diameter influence corneal cell phenotype and matrix synthesis, thereby affecting wound healing. Our studies demonstrated that collagen fibril topography does promote the quiescent keratocyte phenotype and downregulate matrix production thus affecting regenerative wound healing in the cornea. Future studies in this project will focus on using free standing collagen membranes stacked orthogonally one on top of the other to mimic the ordered stacking of the lamellae in the stroma, in order to build a tissue engineered stromal replacement.

As an extension of the corneal wound healing project, we focused on using the nanopatterned collagen substrates for reducing scar formation in the skin, particularly in the case of keloid scars. Keloids are locally aggressive scars characterized by exuberant cell proliferation and matrix synthesis. Current treatments for keloid are ineffective as they are faced with high rates of recurrence. We showed that the presence of aligned collagen fibrils could reduce cell growth and downregulate the production of matrix proteins in keloid fibroblast populations. These results hold promise for the development of a collagen patch using free standing nanopatterned collagen membranes. The collagen patch could inhibit scar growth and thus aid in the design of an effective treatment for keloid that prevents their recurrence. Another area of study is to investigate potential mechanisms involved in regulating cell response to nanotopography. We hope that the understanding gained from these studies could be applied for other tissue engineered implants and devices and contribute to the development of a broad range of clinical applications in the future.

REFERENCES

1.   Desai TA, Hansford D, Ferrari M. Characterization of micromachined silicon membranes for immunoisolation and bioseparation applications. J. Membr. Sci. 1999;159:221-231.

2.   Santiesteban FMM, Swanson SD, Noll DC, Anderson DJ. Magnetic resonance compatibility of multichannel silicon microelectrode systems for neural recording and stimulation: Design criteria, tests, and recommendations. IEEE Trans. Biomed. Eng. 2006;53:547-558.

3.   Ferrara LA, Fleischman AJ, Togawa D, Bauer TW, Benzel EC, Roy S. An in vivo biocompatibility assessment of mems materials for spinal fusion monitoring. Biomed. Microdevices. 2003;5:297-302.

4.   Fissell WH, Fleischman AJ, Humes HD, Roy S. Development of continuous implantable renal replacement: Past and future. Transl. Res. 2007;150:327-336.

5.   Lopez CA, Fleischman AJ, Roy S, Desai TA. Evaluation of silicon nanoporous membranes and ecm-based microenvironments on neurosecretory cells. Biomaterials. 2006;27:3075-3083.

6.   Erlenkötter A, Endres P, Nederlof B, Hornig C, Vienken J. Score model for the evaluation of dialysis membrane hemocompatibility. Artif. Organs. 2008;32:962 - 969.

7.   Papra A, Gadegaard N, Larsen NB. Characterization of ultrathin poly(ethylene glycol) monolayers on silicon substrates. Langmuir. 2001;17:1457-1460.

8.   Fissell WH, Dubnisheva A, Eldridge AN, Fleischman AJ, Zydney AL, Roy S. High-performance silicon nanopore hemofiltration membranes. J. Membr. Sci. 2009;326:58-63.

9.   Popat KC, Desai TA. Poly(ethylene glycol) interfaces: An approach for enhanced performance of microfluidic systems. Biosens. Bioelectron. 2004;19:1037-1044.

10.   Sharma S, Johnson RW, Desai TA. Evaluation of the stability of nonfouling ultrathin poly(ethylene glycol) films for silicon-based microdevices. Langmuir. 2003;20:348-356.

11.   Gupta AS, Wang S, Link E, Anderson EH, Hofmann C, Lewandowski J, Kottke-Marchant K, Marchant RE. Glycocalyx-mimetic dextran-modified poly(vinyl amine) surfactant coating reduces platelet adhesion on medical-grade polycarbonate surface. Biomaterials. 2006;27:3084-95.

12.   Chang Y, Liao SC, Higuchi A, Ruaan RC, Chu CW, Chen WY. A highly stable nonbiofouling surface with well-packed grafted zwitterionic polysulfobetaine for plasma protein repulsion. Langmuir. 2008;24:5453-5458.

13.   Zhang F, Kang ET, Neoh KG, Wang P, Tan KL. Modification of si(100) surface by the grafting of poly(ethylene glycol) for reduction in protein adsorption and platelet adhesion. J. Biomed. Mater. Res. 2001;56:324-332.

14.   Weisenberg BA, Mooradian DL. Hemocompatibility of materials used in microelectromechanical systems: Platelet adhesion and morphology in vitro. J. Biomed. Mater. Res. 2002;60:283-291.

15. Jung YG, Kim HY, Dhong HJ, Park KN, Lee HJ, Lim YJ, Min JY. Ultrasonographic monitoring of implant thickness after augmentation rhinoplasty with expanded polytetrafluoroethylene. Am. J. Rhinol. Allergy. 2009;23:105-110.

16. Kenny D, Hamilton MC, Martin RP. Stainless steel stents and magnetic resonance imaging looking into a black hole. J. Am. Coll. Cardiol. 2009;54:2202-2203.

17. Streller U, Sperling C, Hübner J, Hanke R, Werner C. Design and evaluation of novel blood incubation systems for in vitro hemocompatibility assessment of planar solid surfaces. J. Biomed. Mater. Res., Part B. 2003;66:379-390.

18. Yoshioka T, Tsuru K, Hayakawa S, Osaka A. Blood compatibility of stainless-steel and titanium immobilized with alginic acid layers. Mat. Res. Soc. Symp. Proc. 2003..

19. Schultze G, Hollmann S, Sinah P. Formation of thrombin-antithrombin iii complex using polyamide and hemophan dialyzers. Int. J. Artif. Organs. 1992;15:370-373.

20. Nilsson PH, Engberg AE, Bäck J, Faxälv L, Lindahl TL, Nilsson B, Ekdahl KN. The creation of an antithrombotic surface by apyrase immobilization. Biomaterials. 2010;31:4484-4491.

21. Li L, Marchant RE, Dubnisheva A, Roy S, Fissell WH. Anti-biofouling sulfobetaine polymer thin films on silicon and silicon nanopore membranes. J. Biomater. Sci., Polym. Ed. 2011;22:91-106.

22. Li L, Zhu J, Marchant RE, Roy S, Fissell WH. Biomimetic non-adhesive oligosaccharide surfactant polymer on silicon nanopore membranes for hemofiltration. J. Biomed. Mater. Res., Part A. 2010;In press.

23. Gouzy MF, Sperling C, Salchert K, Pompe T, Streller U, Uhlmann P, Rauwolf C, Simon F, Böhme F, Voit B and others. In vitro blood compatibility of polymeric biomaterials through covalent immobilization of an amidine derivative. Biomaterials. 2004;25:3493-3501.

24. Sperling C, Fischer M, Maitz MF, Werner C. Blood coagulation on biomaterials requires the combination of distinct activation processes. Biomaterials. 2009;30:4447-4456.

25. Hirsh J, Raschke R, Warkentin TE, Dalen JE, Deykin D, Poller L. Heparin: Mechanism of action, pharmacokinetics, dosing considerations, monitoring, efficacy, and safety. Chest. 1995;108:258S-275S.

26. Sinitsyn VV, Bokchubaev ET, Mamontova AG, Ovtrakht NV, Nasonov EL, Konovalov GA, Kukharchuk VV. C3a and c5a anaphylatoxins bind to heparin-based sorbent in low density lipoprotein apheresis: In vitro and in vivo investigations. Artif. Organs. 1992;16:291-293.

27. Phillips DR, Teng W, Arfsten A, Nannizzi-Alaimo L, White MM, Longhurst C, Shattil SJ, Randolph A, Jakubowski JA, Jennings LK and others. Effect of ca2+ on gp iib-iiia interactions with integrilin: Enhanced gp iib-iiia binding and inhibition of platelet aggregation by reductions in the concentration of ionized calcium in plasma anticoagulated with citrate. Circulation. 1997;96:1488-1494.

28. Bergseth G, Lappegård K, Videm V, Mollnes TE. A novel enzyme immunoassay for plasma thrombospondin: Comparison with beta-thromboglobulin as platelet activation marker in vitro and in vivo. Thromb. Res. 2000;99:41-50.

29. Macey M, Azam U, McCarthy D, Webb L, Chapman ES, Okrongly D, Zelmanovic D, Newland A. Evaluation of the anticoagulants edta and citrate, theophylline, adenosine, and dipyridamole (ctad) for assessing platelet activation on the advia 120 hematology system. Clin. Chem. 2002;48:891-899.

30. ISO. Biological evaluation of medical devices: Part 4 - selection of tests for interactions with the blood. 2002.

31. Hong J, Nilsson EK, Reynolds H, Larsson R, Nilsson B. A new in vitro model to study interaction between whole blood and biomaterials. Studies of platelet and coagulation activation and the effect of aspirin. Biomaterials. 1999;20:603-611.

32. Ferraz N, Karlsson OM, Hong J. Time sequence of blood activation by nanoporous alumina: Studies on platelets and complement system. Microsc. Res. Tech. 2010;73(12):1101-1109.

33. Josefsson EC, Hartwig JH, Hoffmeister KM. Platelet storage temperature - how low can we go? Transfus. Med. Hemother. 2007;34:253-261.

34. Rumjantseva V, Hoffmeister KM. Novel and unexpected clearance mechanisms for cold platelets. Transfus. Apher. Sci. 2010;42:63-70.

35. Melvin ME, Fissell WH, Roy S, Brown DL. Silicon induces minimal thromboinflammatory response during 28-day intravascular implant testing. ASAIO J. 2010;56:344-348.

36. Ruberti JW, Zieske JD. Prelude to corneal tissue engineering - gaining control of collagen organization. Prog. Retin. Eye Res. 2008;27:549-577.

37.   Phu D, Wray LS, Warren RV, Haskell RC, Orwin EJ. . Effect of substrate composition and alignment on corneal cell phenotype. Tissue Eng. Part A. 2011;17:799-807.

38.   Crabb RA, Chau EP, Evans MC, Barocas VH, Hubel A. Biomechanical and microstructural characteristics of a collagen film-based corneal stroma equivalent. Tissue Eng. 2006;12:1565-1575.

39.   Torbet J, Malbouyres M, Builles N, Justin V, Roulet M, Damour O, Oldberg Å, Ruggiero F, Hulmes DJS. Orthogonal scaffold of magnetically aligned collagen lamellae for corneal stroma reconstruction. Biomaterials. 2007;28:4268-4276.

40.   Liu W, Merrett K, Griffith M, Fagerholm P, Dravida S, Heyne B, Scaiano JC, Watsky MA, Shinozaki N, Lagali N and others. Recombinant human collagen for tissue engineered corneal substitutes. Biomaterials 2008;29:1147-1158.

41.   Fini ME, Stramer BM. How the cornea heals: Cornea-specific repair mechanisms affecting surgical outcomes. Cornea. 2005;24(8) Supplement:S2-S11.

42.   Jester JV. Corneal crystallins and the development of cellular transparency. Semin. Cell Dev. Biol. 2008;19:82-93.

43.   Fini ME. Keratocyte and fibroblast phenotypes in the repairing cornea. Prog. Retin. Eye Res. 1999;18:529-551.

44.   Pot SA, Liliensiek SJ, Myrna KE, Bentley E, Jester JV, Nealey PF, Murphy CJ. Nanoscale topography-induced modulation of fundamental cell behaviors of rabbit corneal keratocytes, fibroblasts, and myofibroblasts. Invest. Ophthalmol. Vis. Sci. 2010;51:1373-1381.

45. Vrana E, Builles N, Hindie M, Damour O, Aydinli A, Hasirci V. Contact guidance enhances the quality of a tissue engineered corneal stroma. J. Biomed. Mater. Res. A. 2008;84A:454-463.

46. Teixeira AI, Nealey PF, Murphy CJ. Responses of human keratocytes to micro- and nanostructured substrates. J. Biomed. Mater. Res. Part A. 2004;71A:369-376.

47. Berryhill BL, Kader R, Kane B, Birk DE, Feng J, Hassell JR. Partial restoration of the keratocyte phenotype to bovine keratocytes made fibroblastic by serum. Invest. Ophthalmol. Vis. Sci. 2002;43:3416-3421.

48. Freed AD, Doehring TC. Elastic model for crimped collagen fibrils. J. Biomech. Eng. 2005;127:587-593.

49. Paukshto M, McMurtry D, Martin G, Zaitseva T, Bobrov Y. Biocomposites and methods of making the same. US Patent Publication No. WO/2010/019625. 2010.

50. Kirkwood JE, Fuller GG. Liquid crystalline collagen: A self-assembled morphology for the orientation of mammalian cells. Langmuir. 2009;25:3200-3206.

51. Paukshto M, McMurtry D, Bobrov Y, Sableman E. Oriented collagen-based materials, films and methods of making same. US Patent Publication No. WO/2008/131293. 2008.

52. Paukshto M, Fuller G, Michailov A, Remizov S. Optics of sheared liquid-crystal polarizer based on aqueous dispersion of dichroic-dye nano-aggregates. J. Soc. Inf. Display. 2005;13: 765-772.

53. Ukai Y, Ohyama T, Fennell L, Kato Y, Paukshto M, Smith P, Yamashita O, Nakanishi S. Current status and future prospect of in-cell polarizer technology. SID Symposium Digest of Technical Papers. 2004;35:1170-1173.

54. Bobrov Y, Fennell L, Lazarev P, Paukshto M, Remizov S. Manufacturing of a thin-film lcd. Journal of the SID. 2002;10.4:317-321.

55. Fennel L, Lazarev P, Ohmura S, and Paukshto M. Thin crystal film polarizers. Asia display/idw'01. Proceedings of The 21st International Display Research Conference in conjunction with The 8th International Display Workshops. 2001;601-603.

56. Lazarev P, Paukshto M, Sidorenco EN. Self-assembly optical components. Mat. Res. Soc. Symp. Proc. 2003;771:327-332.

57. McMurtry D, Pakshto M, Bobrov Y. A liquid film applicator assembly and rectilinear shearing system incorporating the same. US Patent Publication No. WO/2008/063631. 2008.

58. Thakar RG, Chown MG, Patel A, Peng L, Kumar S, Desai TA. Contractility-dependent modulation of cell proliferation and adhesion by microscale topographical cues. Small. 2008;4:1416-1424.

59. Funderburgh JL, Mann MM, Funderburgh ML. Keratocyte phenotype mediates proteoglycan structure. J. Biol. Chem. 2003;278:45629-45637.

60. Ayala P, Lopez JI, Desai T. Microtopographical cues in 3d attenuate fibrotic phenotype and extracellular matrix deposition: Implications for tissue regeneration. Tissue Eng. Part A. 2010;16:2519-2527.

61. Zhang L, Deng M, Kao CW, Kao WW, Xia Y. Mek kinase 1 regulates c-jun phosphorylation in the control of corneal morphogenesis. Mol Vis. 2003;9:584-593.

62. Hocevar BA, Brown TL, Howe PH. Tgf-[beta] induces fibronectin synthesis through a c-jun n-terminal kinase-dependent, smad4-independent pathway. EMBO J. 1999;18:1345-1356.

63. McCally RL, Freund DE, Zorn A, Bonney-Ray J, Grebe R, de la Cruz Z, Green WR. Light-scattering and ultrastructure of healed penetrating corneal wounds. Invest. Ophthalmol. Vis. Sci. 2007;48:157-165.

64. Kamma-Lorger CS, Boote C, Hayes S, Albon J, Boulton ME, Meek KM. Collagen ultrastructural changes during stromal wound healing in organ cultured bovine corneas. Exp. Eye Res. 2009;88:953-959.

65. Connon CJ, Meek KM. Organization of corneal collagen fibrils during the healing of trephined wounds in rabbits. Wound Repair Regen. 2003;11:71-78.

66. Maurice DM. The structure and transparency of the cornea. J. Physiol. 1957;136:263-286.

67. Benedek GB. Theory of transparency of the eye. Appl. Opt. 1971;10:459-473.

68. Goldman JN, Benedek GB. The relationship between morphology and transparency in the nonswelling corneal stroma of the shark. Invest. Ophthalmol. Vis. Sci. 1967;6:574-600.

69. Shih B, Garside E, McGrouther DA, Bayat A. Molecular dissection of abnormal wound healing processes resulting in keloid disease. Wound Repair Regen. 2010;18:139-153.

70. Atiyeh BS, Costagliola M, Hayek SN. Keloid or hypertrophic scar: The controversy: Review of the literature. Ann. Plast. Surg. 2005;54:676-680.

71. Ong CT, Khoo YT, Mukhopadhyay A, Do DV, Lim IJ, Aalami O, Phan TT. Mtor as a potential therapeutic target for treatment of keloids and excessive scars. Exp. Dermatol. 2007;16:394-404.

72. Atiyeh B. Nonsurgical management of hypertrophic scars: Evidence-based therapies, standard practices, and emerging methods. Aesthetic Plast. Surg. 2007;31:468-492.

73. Seifert O, Bayat A, Geffers R, Dienus K, Buer J, Löfgren S, Matussek A. Identification of unique gene expression patterns within different lesional sites of keloids. Wound Repair Regen. 2008;16:254-265.

74. Appleton I, Brown NJ, Willoughby DA. Apoptosis, necrosis, and proliferation: Possible implications in the etiology of keloids. Am. J. Pathol. 1996;149:1441-1447.

75. Verhaegen PD, Van Zuijlen PP, Pennings NM, Van Marle J, Niessen FB, Van Der Horst CM, Middelkoop E. Differences in collagen architecture between keloid, hypertrophic scar, normotrophic scar, and normal skin: An objective histopathological analysis. Wound Repair Regen. 2009;17:649-656.

76. Al-Attar A, Mess S, Thomassen JM, Kauffman CL, SP D. Keloid pathogenesis and treatment. Plast Reconstr. Surg. 2006;117:286-300.

77. Har-Shai Y, Amar M, Sabo E. Intralesional cryotherapy for enhancing the involution of hypertrophic scars and keloids. Plast. Reconstr. Surg. 2003;111:1841-1852.

78. Parkinson LG, Rea SM, Stevenson AW, Wood FM, Fear MW. The effect of nano-scale topography on keratinocyte phenotype and wound healing following burn injury. Tissue Eng. Part A 2012;18:703-714.

79. Muthusubramaniam L, Peng L, Zaitseva T, Paukshto M, Martin GR, Desai TA. Collagen fibril diameter and alignment promote the quiescent keratocyte phenotype. J. Biomed. Mat. Res. Part A. 2011;100A:613-621.

80. Schmults CD, Phelps R, Goldberg DJ. Nonablative facial remodeling: Erythema reduction and histologic evidence of new collagen formation using a 300-microsecond 1064-nm nd:Yag laser. Arch. Dermatol. 2004;140:1373-1376.

81. Smith JC, Boone BE, Opalenik SR, Williams SM, Russell SB. Gene profiling of keloid fibroblasts shows altered expression in multiple fibrosis-associated pathways. J. Invest. Dermatol. 2007;128:1298-1310.

82. Russell SB, Russell JD, Trupin KM, Gayden AE, Opalenik SR, Nanney LB, Broquist AH, Raju L, Williams SM. Epigenetically altered wound healing in keloid fibroblasts. J. Invest. Dermatol. 2010;130:2489-2496.

83. Iyer VR, Eisen MB, Ross DT, Schuler G, Moore T, Lee JCF, Trent JM, Staudt LM, Hudson J, Boguski MS and others. The transcriptional program in the response of human fibroblasts to serum. Science. 1999;283:83-87.

84. Fujiwara M, Muragaki Y, Ooshima A. Keloid-derived fibroblasts show increased secretion of factors involved in collagen turnover and depend on matrix metalloproteinase for migration. Br. J. Dermatol. 2005;153:295-300.

85.   Chen CS, Mrksich M, Huang S, Whitesides GM, Ingber DE. Micropatterned surfaces for control of cell shape, position, and function. Biotechnology Progress. 1998;14:356-363.

86.   Singhvi R, Kumar A, Lopez GP, Stephanopoulos GN, Wang DI, Whitesides GM, DE. I. Engineering cell shape and function. Science. 1994;264:696-698.

87.   Calderon M, Lawrence WT, Banes AJ. Increased proliferation in keloid fibroblasts wounded in vitro. J. Surg. Res. 1996;61:343-347.

88.   Toh PPC, Li JJ, Yip GWC, Lo S-L, Guo C-H, Phan T-T, Bay B-H. Modulation of metallothionein isoforms is associated with collagen deposition in proliferating keloid fibroblasts in vitro. Exp. Dermatol. 2010;19:987-993.

89.   Bettinger DA, Yager DR, Diegelmann RF, IK. C. The effect of tgf-beta on keloid fibroblast proliferation and collagen synthesis. Plast. Reconstr. Surg. 1996;98:827-833.

90.   Stacey DW. Cyclin d1 serves as a cell cycle regulatory switch in actively proliferating cells. Curr. Opin. Cell Biol. 2003;15:158-163.

91.   Chipev CC, Simman R, Hatch G, Katz AE, Siegel DM, M. S. Myofibroblast phenotype and apoptosis in keloid and palmar fibroblasts in vitro. Cell Death Differ. 2000;7:166-176.

92.   Friedman DW, Boyd CD, Mackenzie JW, Norton P, Olson RM, Deak SB. Regulation of collagen gene expression in keloids and hypertrophic scars. J. Surg. Res. 1993;55:214-222.

93.   Syed F, Ahmadi E, Iqbal SA, Singh S, McGrouther DA, Bayat A. Fibroblasts from the growing margin of keloid scars produce higher levels of collagen i and

iii compared with intralesional and extralesional sites: Clinical implications for lesional site-directed therapy. Br. J. Dermatol. 2011;164:83-96.

94.   Imaizumi R, Akasaka Y, Inomata N, Okada E, Ito K, Ishikawa Y, Maruyama Y. Promoted activation of matrix metalloproteinase (mmp)-2 in keloid fibroblasts and increased expression of mmp-2 in collagen bundle regions: Implications for mechanisms of keloid progression. Histopathology. 2009;54:722-730.

95.   Meller D, Peters K, Meller K. Human cornea and sclera studied by atomic force microscopy. Cell Tissue Res. 1997;288:111-118.
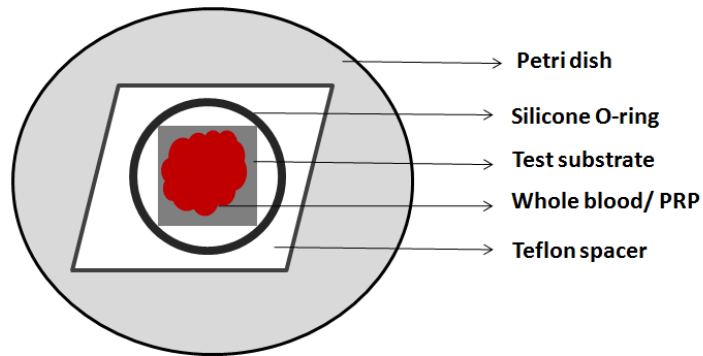
Figure S2.1. Schematic representation of the test substrate placed on a Teflon spacer for whole blood or platelet rich plasma incubation.
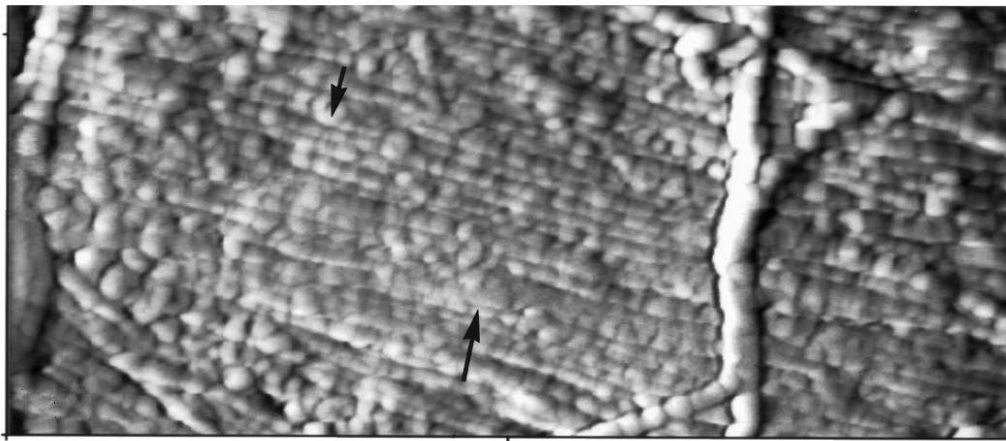

Figure S3.1. AFM image of human cornea. The stacked corneal collagen fibrils (fine arrows) form an almost uniform sheet. Image reproduced from Meller et al.[95]
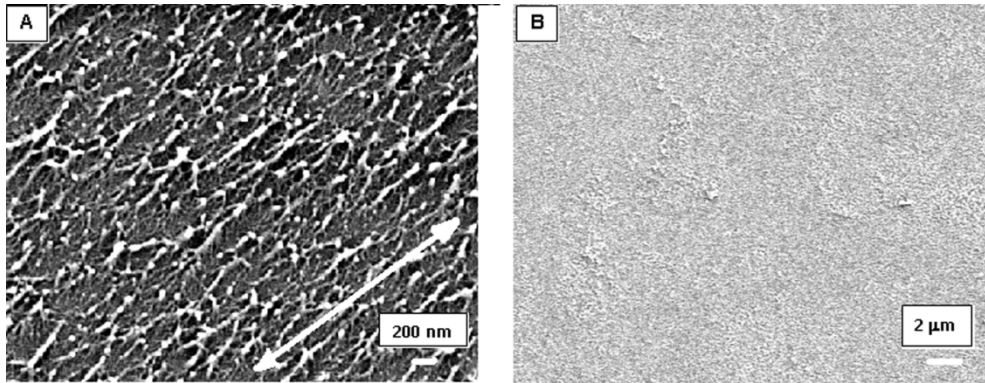
Figure S3.2. Scanning electron microscopy image showing: (A) Fibril arrangement after cell seeding on 30A substrate. Arrow indicates fibril direction. (B) Flat collagen coated glass with no fibrils after cell seeding on the FC substrate.
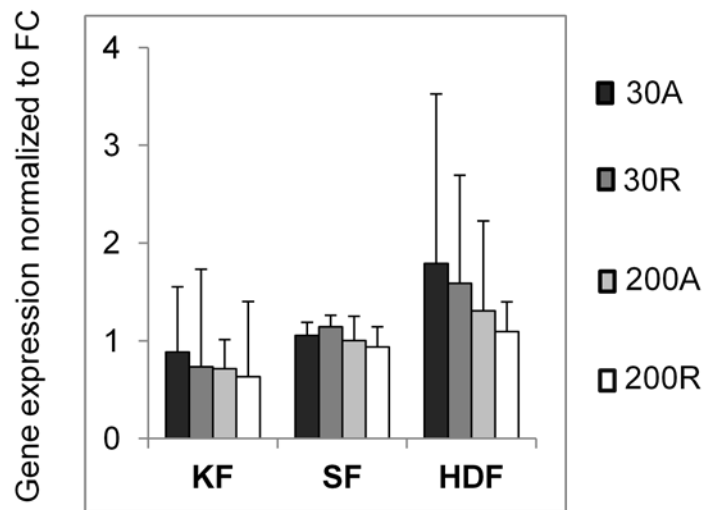

FIGURE S4.1. Fibril alignment (30A) reduced gene expression of MMP-1 in KF alone. Data is presented as mean $\pm$ SD, using three to five replicates per substrate.

Publishing Agreement

It is the policy of the University to encourage the distribution of all theses, dissertations, and manuscripts. Copies of all UCSF theses, dissertations, and manuscripts will be routed to the library via the Graduate Division. The library will make all theses, dissertations, and manuscripts accessible to the public and will preserve these to the best of their abilities, in perpetuity.

I hereby grant permission to the Graduate Division of the University of California, San Francisco to release copies of my thesis, dissertation, or manuscript to the Campus Library to provide access and preservation, in whole or in part, in perpetuity.

Lalitha   2-15-2013

Author Signature   Date